Study of neutral transport and plasma fueling in the HIT-SI3 and HIT-SIU experiments

Joshua Bond Perry

A thesis
submitted in partial fulfillment of the
requirements for the degree of

Master of Science

University of Washington

2022

Reading Committee:
Justin Little, Chair
Christopher Hansen
Uri Shumlak

Program Authorized to Offer Degree:
William E. Boeing Department of Aeronautics and Astronautics

University of Washington

Abstract

Study of neutral transport and plasma fueling in the HIT-SI3 and HIT-SIU experiments

Joshua Bond Perry

Chair of the Supervisory Committee:
Professor Justin Little
Aeronautics and Astronautics

Compared with more conventional toroidal magnetic confinement configurations for fusion plasmas, the spheromak has several favorable properties, among which is the potential to be Ohmicly heated all the way up to ignition temperatures. This would enable more economical fusion power plants. To this end, the HIT-SI family of experiments aim to demonstrate efficient formation and sustainment of spheromaks using Steady Inductive Helicity Injection (SIHI). The previous HIT-SI and HIT-SI3 experiments were limited in performance by high neutral density in the confinement region, and the need to continuously supply neutral gas fueling to the system. In this work the effectiveness of different methods to control neutral and plasma density in this class of devices was studied. Firstly, the performance of a set of existing passive pumping volumes was considered. To gain insight into the performance of these volumes, and the conditions of the edge plasma region, the plasma inside one of these volumes was characterized using a triple Langmuir probe. A 1D plasma-neutral transport model was then created to assess what combinations of edge plasma parameters most closely corresponded to the probe data. Although an exact match could not be achieved, this study suggests high neutral density and strong plasma-neutral coupling in the edge plasma region, which is expected to degrade HIT-SI3 spheromak performance. The subsequent HIT-SIU experiment was designed with several improvements to reduce the buildup of neutral gas and allow greater control of plasma density. One of these is a set of electrodeless plasma sources

intended to ionize the neutral gas used to fuel the helicity injectors. As part of this work, these plasma sources were constructed, installed and characterized. It was determined that they operate as inductively-coupled plasma (ICP) sources and can reliably supply plasma to the helicity injectors over a wide range of density. During preliminary operations on HIT-SIU, these plasma sources were able to improve the speed and reliability of breakdown, as well as the consistency of plasma density. However, energetic plasma-material interactions were also observed, which necessitated removing the sources. A mitigation strategy was developed that will allow the plasma sources to be reinstalled, but in the meantime, HIT-SIU has demonstrated improved density control and performance when compared to its predecessors and is expected to perform even better once the new plasma sources are reinstalled.

TABLE OF CONTENTS

LIST OF FIGURES

GLOSSARY

SIHI: Steady Inductive Helicity Injection

IDCD: Imposed Dynamo Current Drive

HIT-SI: Helicity Injected Torus – Steady Inductive

ITER: International Thermonuclear Experimental Reactor

SSPX: Sustained SPheromak eXperiment

ICP: Inductively-Coupled Plasma

IDS: Ion Doppler Spectroscopy

TALIF: Two-photon Laser Induced Fluorescence

RFP: Reversed-Field Pinch

ACKNOWLEDGMENTS

This work would not have been possible without the support of many people. I would first like to thank Chris Hansen, for doing the work of a professor, despite not having the position. I would also like to specifically thank Kyle Morgan, for always being available and eager to take time to help or explain things to students. Additionally, many aspects of this work are heavily based on the work of Paul Melnik, for the triple Langmuir probe; Eric Meier, Uri Shumlak, and Derek Sutherland, for the plasma-neutral model; and Aaron Hossack, for the optical diagnostics and the original HIT-SI pre-ionization source.

DEDICATION

To my parents, for their constant support and encouragement

Chapter 1

INTRODUCTION

1.1 Motivation

Energy production is fundamental to technological civilization, so much so that the most widely accepted method of classifying hypothetical extraterrestrial civilizations categorizes them by total energy output on a logarithmic scale. On the Kardashev scale, created by russian astronomer Nikolai Kardashev, type one indicates energy use on an planetary scale, type two is energy use on a stellar scale, and type three is energy use on a galactic scale. Humanity would achieve Kardashev type one status at five times its current energy consumption [19]. Per capita energy consumption is also strongly correlated with most metrics of quality of life. Lifting up the entire global population to first world living standards would require nearly doubling global energy production, even more so in the next few decades, since the global population is expected to rise to somewhere between 9 and 13 billion by the end of the century, by UN estimates [2, 29]. Fossil fuels, which currently provide the vast majority of our energy, are simply not up to the task of meeting any of these challenges. Not only are they scarce resources which will be depleted on timescales of decades if aggressive growth continues, but the CO_2 and methane emissions produced as a byproduct of their use threaten to destabilize the planet's climate, with disastrous consequences for much of the world's population [32].

Renewable energy sources like wind and solar avoid these problems, but have some of their own. Their local and seasonal variability means that to provide a larger portion of total energy usage, power grids must be reconfigured to meet their needs or supplemented with large-scale energy storage, both of which make them less cost-effective as they become a larger and larger portion of the total supply of electrical power [33]. Nuclear fission is

one possible solution, since it provides constant power with no CO_2 emissions, from a relatively plentiful resource. However, it has suffered from a series of high-profile accidents which, combined with its potential to be weaponized, lead to a very restrictive regulatory environment, which suppresses innovation and keeps capital costs very high. Compounding this is the contribution to the lifecycle cost of a fission reactor related to managing spent nuclear fuel. Spent nuclear fuel contains a combination of long-lived heavy transuranics and high-radiotoxicity fission products that make it very expensive to reprocess or dispose of in a permanent way. Existing fission reactor technologies also suffer from an inability to quickly ramp power output up and down, due to xenon fission product contamination, making them a far from ideal complement to renewables.

Nuclear fusion has the potential to address all of these problems. However, to produce energy from fusion of the hydrogen isotopes deuterium and tritium, the most viable fusion reaction for power production, the reactants must be near thermal equilibrium at a temperature of several hundred million degrees Kelvin, enough that their kinetic energy can overcome the coulomb barrier that normally prevents strong force interaction between atomic nuclei. Such a thermonuclear reactor, when operating in a breeder mode producing tritium from lithium, would consume an almost negligible amount of two very plentiful resources (hydrogen and lithium), and would produce no greenhouse gas emissions. Although it would produce intense neutron radiation within the reactor, the lack of actinide elements means no long-lived radioactive waste would be created, and since no fissionable materials are involved, the weaponization potential is much lower. Fusion is also expected to better compliment renewables either by throttling up and down or, in pulsed configurations, adjusting the pulse rate. However, for nuclear fusion to be a practical energy source, a fusion reactor needs to be reliable and have low capital and operating costs [22].

1.2 Toroidal Plasma Confinement

Since no physical material can contain matter at thermonuclear temperatures, fusion fuel needs to exist in the form of a plasma contained by electromagnetic forces, or other non-

material means. The most popular class of confinement configurations confines charged particles using magnetic field lines closed into a toroidal shape. These toroidal fields can be created by internal plasma currents, as in spheromaks, by external field coils only, as in stellarators, or by a combination of both, as in tokamaks and field-reversed pinches. These closed fields are ideal for keeping thermal energy from escaping, but make it difficult to add energy to the plasma for the purpose of current drive and heating. Ohmic heating is used on many tokamaks for startup, by ramping up current in a transformer coil to drive current through the plasma, which acts as a secondary coil. However, this method is limited in that it can't operate in a steady-state mode, and becomes less effective at heating at higher plasma temperatures, due to decreasing resistivity. A more versatile method is RF heating, where various types of RF waves are used to heat the plasma [22]. There are a wide variety of variations but many of them suffer from not being able to penetrate beyond the outer layers of the plasma, and/or requiring electrons to transfer energy to the ions through collisions. It can also be used for current drive, but at much lower efficiency. Another method is neutral beam injection, where light ion beams are neutralized, allowing them to penetrate the magnetic fields and re-ionize on the inside, transferring energy to the ions directly. However, high-power neutral particle beams are large, complex, and inefficient devices that are poorly suited to a practical power plant [31]. Figure 1.1 shows the scale of the heating mechanisms for ITER, an upcoming large tokamak under construction in France, which is expected to produce 500 Meagawatts of fusion power.

1.3 The HIT-SI Approach

The Helicity Injected Torus - Steady Inductive experiment (HIT-SI), and its successors HIT-SI3 and HIT-SIU, form and sustain spheromak plasmas using Steady Inductive Helicity Injection (SIHI). This is accomplished with a set of semi-toroidal structures mounted perpendicular to the toroidal confinement volume, each containing a magnetic flux coil and a voltage induction coil, which are oscillated in-phase with each other. This generates, for each injector, a loop of helical field passing through the confinement volume. These loops

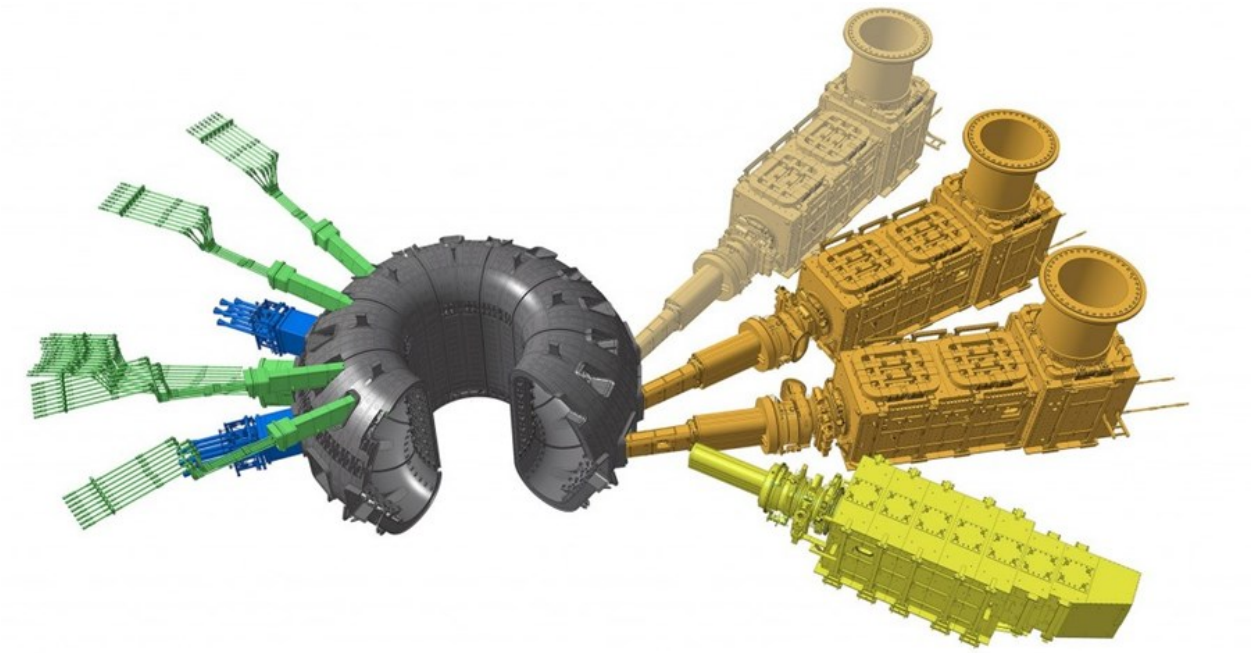

Figure 1.1: Schematic of ITER confinement vessel (gray) with RF heating systems (blue and green) and neutral beam injectors (orange and yellow). [31]

go through a rapid relaxation event which conserves helicity, converting them into a single axisymmetric spheromak state [39]. During the subsequent sustainment phase, the injectors continue to produce non-axisymmetric helical magnetic fields impinging upon on the surface of the spheromak plasma. The goal of this approach is to use the perpendicular magnetic fluctuations imposed by the injector fields to add helicity and energy, driving currents, to the plasma while retaining closed flux surfaces. This process, known as Imposed Dynamo Current Drive (IDCD), is postulated to arise from the tendency of magnetized plasmas to self-organize – relaxing toward a state of minimum energy while conserving helicity [39]. Using inductive helicity injection, IDCD can be very efficient, and can operate in a steady-state mode, by using multiple, phase-shifted helicity injectors [14]. This greatly improves the potential of the spheromak as a rector concept, since they previously could not be sustained without taking advantage of plasma instabilities, which opened magnetic flux surfaces, de-

grading confinement in the process [23]. The primary heating mechanism is Ohmic heating of electrons, but viscous heating of ions is also a major contributor, and this has allowed HIT-SI spheromaks to achieve ion temperatures up to double the electron temperature [14]. In addition to more efficient current drive, spheromaks created and sustained by this method could have several other advantages when compared to the tokamak, the most popular toroidal confinement configuration. Plasma current in tokamaks is limited by the requirement that the toroidal field it produces cannot exceed a certain fraction of the toroidal field applied by external magnets. This field strength is determined by engineering constraints of the superconducting coils themselves, which are massive structures in experiments like ITER. In spheromaks, the toroidal field is produced entirely by plasma current, and poloidal coils are only needed to oppose outward pressure. This makes the engineering constraints of the magnets much less restrictive on the design of a reactor [13].

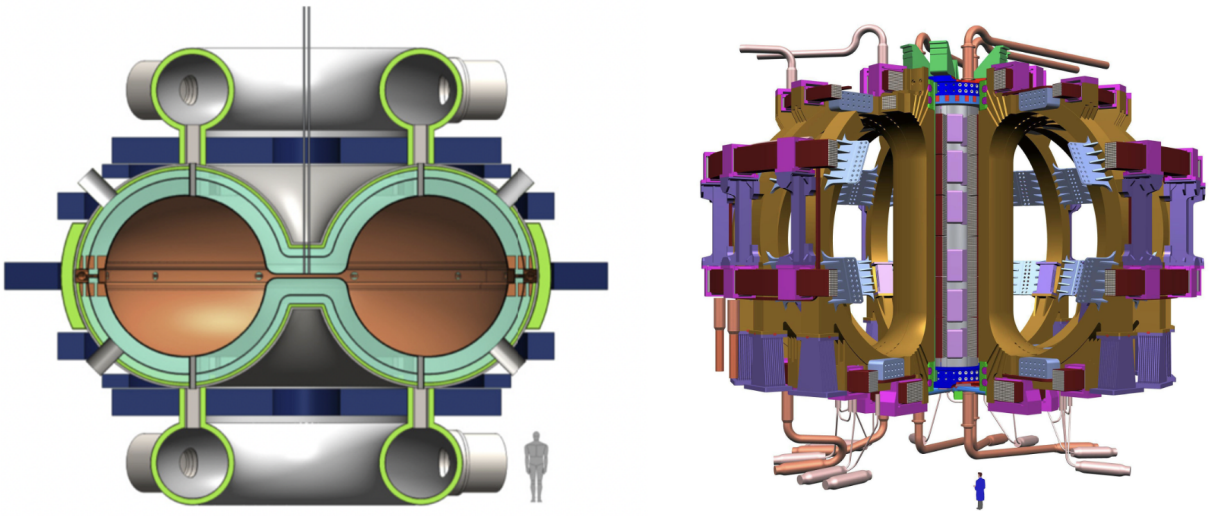

Figure 1.2: Illustration of the "Dynomak" spheromak reactor concept using SIHI (poloidal field coils shown in blue), compared to the magnet assembly for ITER (toroidal field coils in gold and poloidal field coils in red). A two meter human figure is included in both for scale [38].

If SIHI/IDCD is successful at forming and sustaining spheromaks at high enough power, it is conceivable that they could be ohmically heated all the way up to ignition temperatures. In addition to having more current relative to magnetic field in the core of the plasma, a spheromak reactor would also have a higher average beta (β). β is the ratio of magnetic field pressure to plasma pressure, one formulation of which is given by equation 1.1, where the magnetic field strength at a single location (eg. magnetic axis or edge) B_0 is used.

$$< \beta >= \frac{< P >}{B_0^2} 2\mu_0 \tag{1.1}$$

For both of these reasons, it would contain a higher density plasma relative to externally applied fields, and thus be much more compact. Active control of helicity injector phasing may also provide improved current profile control, helping to mitigate any instabilities that may appear at higher energy densities.

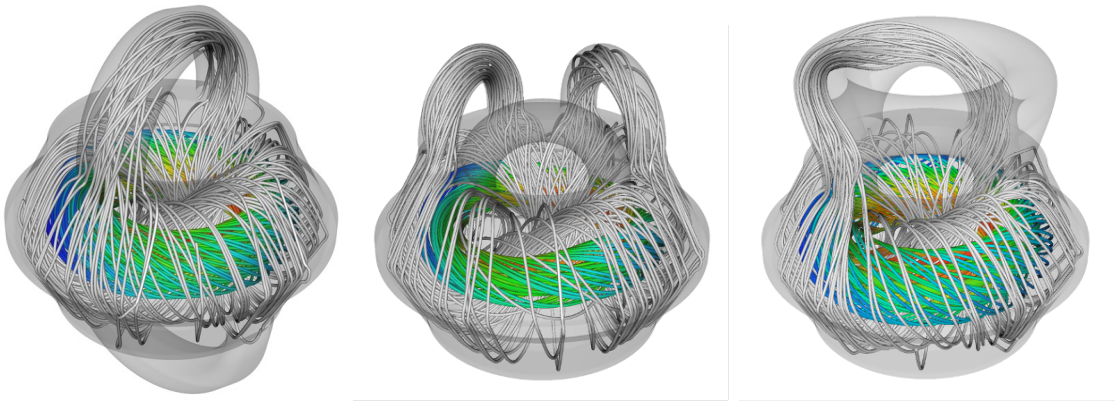

Figure 1.3: Diagram of representative magnetic field lines in HIT-SI (left), HIT-SI3 (center) and HIT-SIU (right). Spheromak flux surfaces are highlighted in color and the external injector field lines are shown in gray [26].

The original HIT-SI experiment was a testbed to prove the efficacy of steady inductive helicity injection and used two injectors on opposite sides of the confinement volume, phased 90° apart from each other, as shown in figure 1.3. The second iteration, HIT-SI3, used

three injectors all on the same side of the machine and phased 120° apart from each other. It was constructed primarily to explore active control of spheromak rotation by controlling injector phasing [15]. The third and most recent iteration of this experiment, HIT-SIU, uses four injectors, merged into a helicity injection manifold. The manifold allows the injectors to excite different and more varied combinations of toroidal modes. They are also able to operate as a plasma torus separate from the main confinement volume, similar to a tokamak, before transitioning to form a spheromak as normal. This may help to form spheromaks with higher initial current, as well as aiding in initial breakdown. Another improvement is in the larger size of the injectors, which reduces heat flux on the interior surfaces and reduces the chance of energetic plasma-material interactions.

1.4 Density Reduction and Control

One of the biggest obstacles to increasing current drive performance in HIT-SI and HIT-SI3 has been the buildup of plasma density and neutral gas in the confinement volume. These experiments used gas puff valves to fuel the injectors, relying on Paschen breakdown to ionize the gas initially. The injectors also displayed a tendency to expel plasma inside, meaning it needed to be replenished by injecting more neutral gas, otherwise the current that the injectors are able to generate becomes density-limited [35]. Constantly injecting neutral gas into the injectors causes it to build up in the confinement volume, bleeding energy away from the plasma through charge-exchange, ionization and scattering, degrading current drive performance [37] in the process. The Paschen criteria also limits what plasma density can be achieved in the confinement volume. In a spheromak, density in the confinement volume must be controlled to optimize current drive performance. The j/n parameter for spheromaks should ideally be above the Greenwald limit, but many HIT-SI and HIT-SI3 discharges stay far below this limit. To partially mitigate this, HIT-SI and HIT-SI3 used a hygroscopic alumina coating on the walls, and passive pumping volumes designed to relieve neutral pressure, but these measures were of limited effectiveness for the desired duration [15]. An inductively-coupled plasma source was added to the confinement volume, to help ionize gas in

the confinement volume, with some improvement, but for HIT-SIU, the puff valves supplying the injectors were supplemented with high-power inductively-coupled plasma sources, to pre-ionize gas going into the injectors, and get around the limits in density previously imposed by the Paschen criteria. In addition to minimizing energy loss to neutrals, The sources on HIT-SIU aim to enable more precise control of the plasma density to fine tune the j/n parameter. If successful, this will inform the design of a future proof-of-principle experiment HIT-POP, which will aim to demonstrate closed flux surfaces and significant steady-state pressure confinement [38].

Chapter 2

NEUTRAL PASSIVE PUMPING STUDY IN HIT-SI3

HIT-SI3 employed passive pumping volumes to control neutral density in the confinement region. They are four cylinders of approximately 1 meter in length and 20 cm in diameter, mounted to the side opposite the injectors. A set of copper louvers, pictured in 2.1, allow toroidal currents to continue to flow in the flux conserver. The effectiveness of these volumes depends on the transport properties of the edge plasma region of the confinement volume, meaning that measurements of the plasma inside these volumes also can provide information on the behavior of the edge region, where it is undesirable to use perturbative diagnostics. To this end, a fast ionization pressure gauge and a triple Langmuir probe were fitted to two of the volumes, with the gauge fixed to a location near the far end of the cylinder, and the probe is able to traverse up to 17 cm back from the edge of the louvers. Since the data collected from a Langmuir probe is limited and prone to biases, a numerical model of the system was created, to compare several assumptions of the edge plasma parameters to the probe data.

2.1 Pressure Gauge Study

To get a rough idea of how the presence of the spheromak plasma affects neutral transport, a hot-cathode ionization pressure gauge was employed, at the end of one of the pumping volumes. These gauges use a hot cathode at the top of a potential well to create an electron cloud. Neutral gas impinging on it is ionized and accelerated towards a collection grid. Figure 2.2 displays the neutral pressure at this gauge with the helicity injectors on and off (with and without a plasma).

With the plasma present, neutral transport is enhanced by multiple orders of magnitude,

Figure 2.1: Louvers on HIT-SI3, dividing the confinement volume (copper) from the pumping volumes (gray).

rising by the end of the discharge to approximately 1.4×10^{20} m^{-3}. Both curves closely match exponential growth, with the growth constant being approximately 2.8×10^{3} higher in the plasma case. This suggests that the time for pressure waves to travel from the puff valves to the pressure gauge (approximately 1.5 meters) is negligible on the time scales measured, and pressure is rising as neutral density and/or temperature is increasing. There are several possible reasons for this. Firstly, there is far more thermal energy in the system when the injectors are running, and thermal exchange with the plasma will likely heat the gas considerably. Also, as plasma in the edge region flows into the pumping volume, it will collide with the walls and be neutralized. This could be a major contributor to the pressure as seen by the gauge, since it is expected to move through the system much faster, due to higher temperature and that momentum is transferred between particles by electromagnetic forces instead of collisions. Finally, there could be a combination of the two processes, if there is strong plasma-neutral coupling. Plasma pressure and heating could raise the neutral pressure simultaneously to significant wall recycling. From the perspective of achieving high-performance spheromak discharges, it is preferable that neutrals entering the pumping volume are as small of a contributor as possible, since that indicates lower neutral density

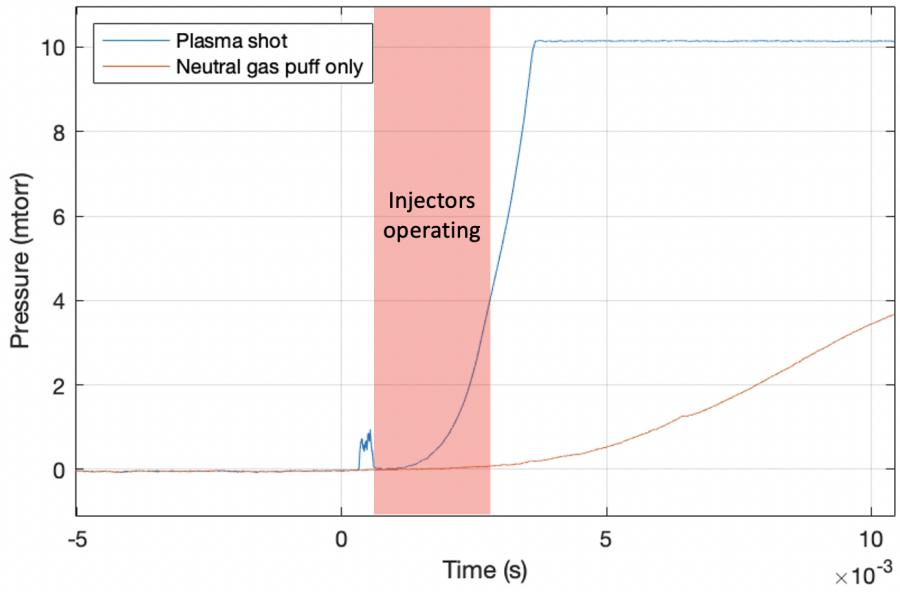

Figure 2.2: Neutral pressure at the far end of a pumping volume with (blue) and without (red) plasma. The blue curve levels out due to the signal saturating the input on the data acquisition system. The spike before the injectors turn on is noise due to operation of a plasma source intended to aid ionization.

in the confinement volume. Conversely, if neutral density is high, it will degrade spheromak performance through ionization and charge-exchange losses, and if neutral buildup continues long enough, it could eventually quench the plasma entirely, although this was not observed during HIT-SI3 operation.

2.2 Langmuir Probe Study

To better characterize the edge plasma and the role of the pumping volumes, a triple Langmuir probe was employed inside one of the volumes, with a 17 cm traverse distance back from the edge of the louvers.

A triple Langmuir probe uses two probe tips set at a constant voltage difference and a third floating probe tip. The electron temperature and density are determined from currents

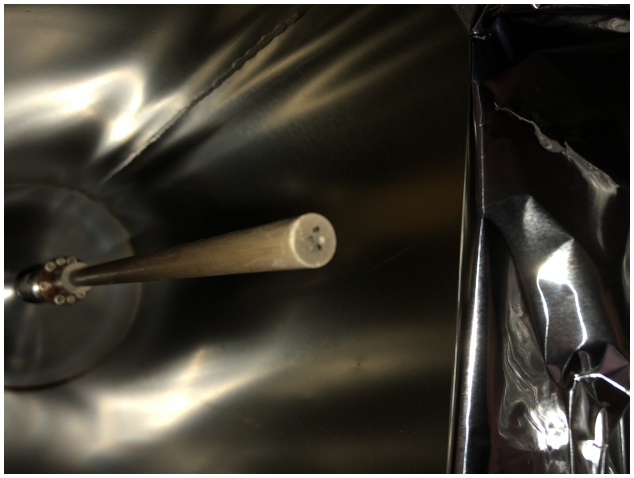

Figure 2.3: Image of triple probe tips inside pumping volume.

measured on the three probe tips. For probe tips 1 and 2 connected ($I_1 = -I_2$), and probe 3 floating ($I_f = 0$) the probe current is given by

$$I_p = I_{i0} + I_{e0} \exp(\frac{V_p}{T_e}). \tag{2.1}$$

Since $I_{i0} = -I_{e0}$, T_e can be found by dividing I_1 by I_2

$$-1 = \frac{1 - \exp(\frac{V_1}{T_e})}{1 - \exp(\frac{V_1}{T_e})}. \tag{2.2}$$

Expanding and substituting in the term $\exp(\frac{V_f}{T_e}) = 1$ gives

$$(\exp(\frac{V_1 - V_f}{T_e}) - 1) = \exp(\frac{V_1 - V_2}{T_e}) - \exp(\frac{V_1 - V_f}{T_e}), \tag{2.3}$$

which simplifies to

$$2\exp(\frac{V_f - V_1}{T_e}) = 1 + \exp(\frac{V_2 - V_1}{T_e}). \tag{2.4}$$

The electron temperature is then given by eq 2.5

$$T_e = \frac{V_1 - V_f}{-\ln(\frac{1}{2}(1 + \exp(\frac{V_2 - V_1}{T_e}))}), \tag{2.5}$$

where the term $\exp(\frac{V_2-V_1}{T_e})$ is usually neglected with the assumption that $V_2 - V_1 >> T_e$. Electron density is calculated using the electron temperature and the ion saturation current. In the same way as a double Langmuir probe , it is given by

$$n_e = \frac{I_{i0}}{0.61Ae\sqrt{\frac{kT_e}{m_i}}} \tag{2.6}$$

Where the ion saturation current is also found in the same manner as a double probe

$$I_{i0} = \frac{I_1}{\tanh\left(\frac{V_2-V_1}{2T_e}\right)} \tag{2.7}$$

The tanh term then converges to 1 for $V_2 - V_1 >> T_e$

The error from the $\exp(\frac{V_2-V_1}{T_e})$ term in the temperature calculation can be minimized either by raising the potential difference applied to the probe tips, or by iterating equation 2.5 several times. For this study, the voltage applied to the probes was raised to approximately 68 V, which is 5 times the electron temperature that the probe results converged to. As seen in figure 2.4, that is more than sufficient to make the error from excluding this term negligible [28].

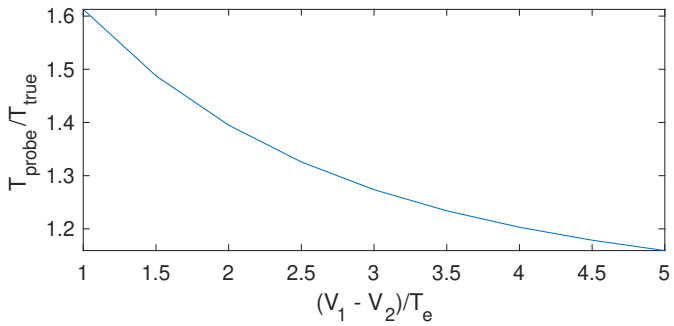

Figure 2.4: Convergence of electron temperature, as read by the triple probe, as applied voltage is increased.

Another potential issue with using a Langmuir probe in this way is that the plasma is flowing into the pumping volume, during at least the first phase of the discharge. However,

since the ion saturation current factors out of the expression for electron temperature in the triple probe, it is unaffected [28]. The density reading, however, is affected in the same manner as in a Mach probe. To get an estimate for the flow velocity, the time for the plasma to reach the probe was measured by the difference between the rise time of the toroidal current and the voltage on the floating probe. As seen in 2.5, there is an apparent linear trend. Fitting a constant flow velocity to this indicates that it is about 63% of the ion acoustic speed obtained, assuming equal ion and electron temperatures and using the electron temperature indicated by the probe [17].

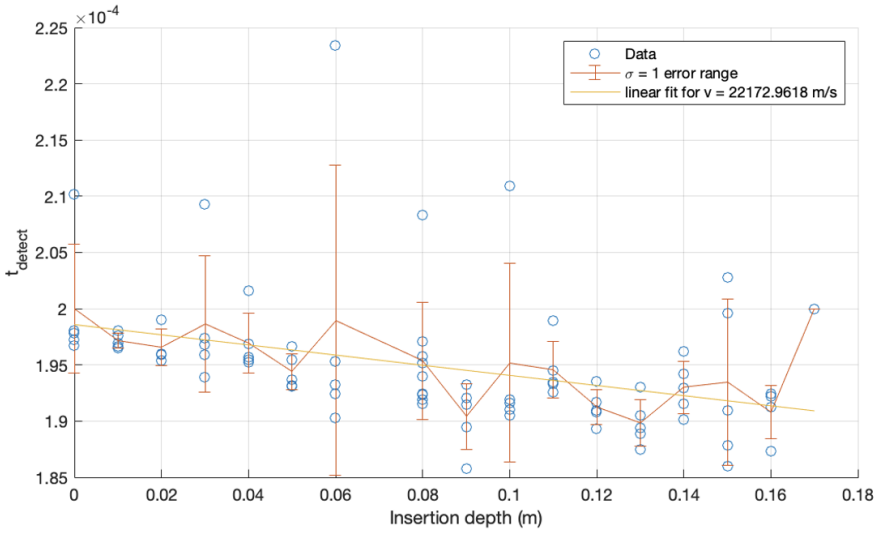

Figure 2.5: Plot of probe position and time for the probe to detect plasma, with linear fit indicating an initial flow velocity.

This velocity can be used to estimate a correction factor for the probe current by doing the analysis for a Mach probe in reverse. Since the plasma flow is impacting the cylindrical probe tips head-on, a planar probe is a more appropriate approximation than a side-on cylindrical probe. A kinetic model of such a configuration was developed by Chung in 1990, and his more recent review paper shows it gives similar results to another developed by Hutchinson, and greatly deviates from some of the fluid models [6, 7].

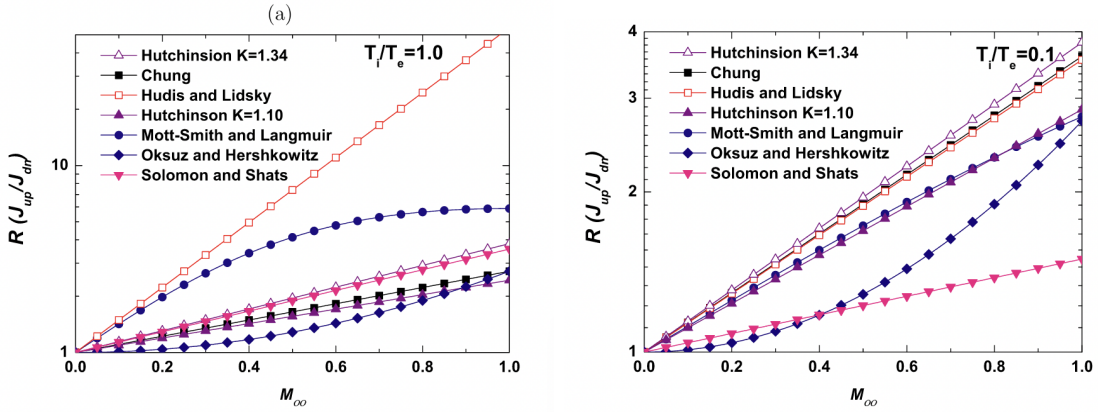

Figure 2.6: Plots from Chung 2012 of Mach probe correction factors with equal electron and ion temperatures (left) and higher electron temperature (right) [7]

Figure 2.6 shows the Mach probe current ratio as a function of subsonic Mach number, given by several different models examined by Chung's 2012 review paper [7]. For cases of equal electron and ion temperature, and for a case of hot electrons. Assuming the equilibrium case, the current ratio is 1.72. When this correction factor is introduced, the steady-state electron temperature and density in the first 17 cm of the pumping volume are displayed in figure 2.7.

The electron temperature is roughly consistent with measurements of impurity temperature from ion Doppler spectroscopy studies, but it is surprising that the plasma does not cool much as it interacts with the cooler neutrals and the chamber walls as it enters the pumping volumes [14]. The density data, however, suggests strong interaction with the walls, with a clear exponential falloff in the density away from the confinement volume. Both readings deviate from those trends very close to the inlet of the pumping volume, likely due to the louvers obstructing the plasma flow.

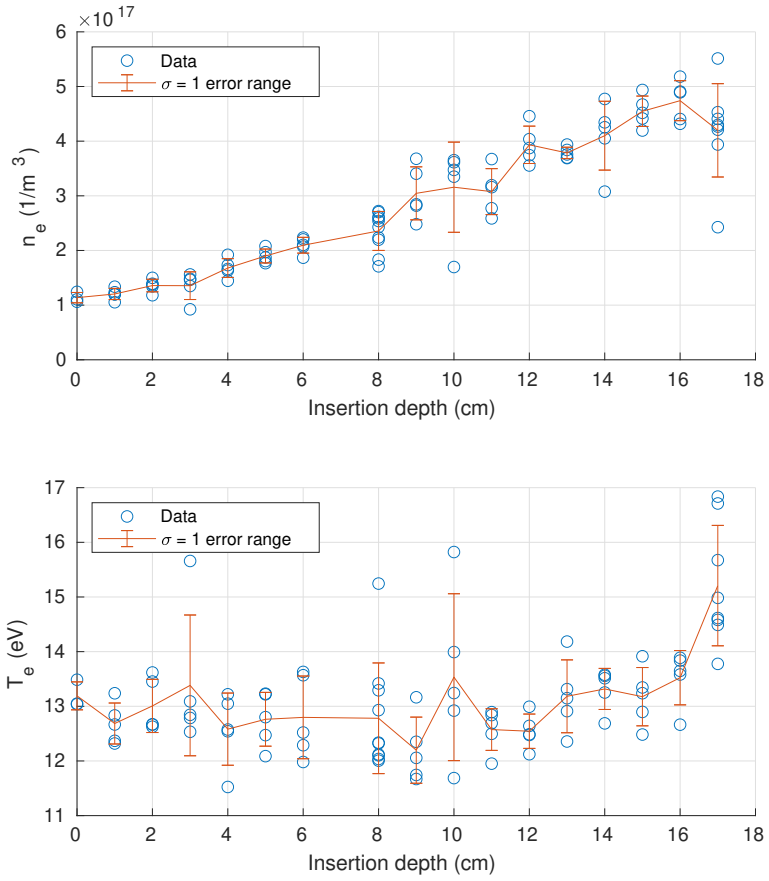

Figure 2.7: Electron density (top) and temperature (bottom) at multiple points inside the pumping volume.

2.3 1-D Plasma-Neutral Transport Model

To predict what we would see in these profiles for various values of the edge plasma parameters, a one-dimensional multifluid advection-diffusion transport model was created, using the method originally given by Meier and Shumlak [24], and elaborated on by Sutherland [37]. The model advances continuity equations for the first three moments of the plasma and neutral fluids, including ionization, recombination, charge-exchange, and wall recycling in a

simplified form. These equations are given by

Zeroth Moment

$$\frac{\partial n_i}{\partial t} = D\frac{\partial^2 n_i}{\partial x^2} - V_i\frac{\partial n_i}{\partial x} + n_i n_n < \sigma_{iz} v_e > - n_i^2 < \sigma_{rc} v_e > - n_i \sigma_{wall} v_{Bohm} \tag{2.8}$$

$$\frac{\partial n_n}{\partial t} = D\frac{\partial^2 n_n}{\partial x^2} - V_n\frac{\partial n_n}{\partial x} - n_i n_n < \sigma_{iz} v_e > + n_i^2 < \sigma_{rc} v_e > + n_i \sigma_{wall} v_{Bohm} \tag{2.9}$$

First Moment

$$\begin{aligned}\frac{\partial V_i}{\partial t} = D\frac{\partial^2 V_i}{\partial x^2} - V_i\frac{\partial V_i}{\partial x} - \frac{2}{m_i n_i}\frac{\partial}{\partial x}(n_i k T_i) \\ + n_n(V_n - V_i)(< \sigma_{iz} v_e > + \sigma_{cx} V_{cx} + r_{in} + r_{ni})\end{aligned} \tag{2.10}$$

$$\begin{aligned}\frac{\partial V_n}{\partial t} = D\frac{\partial^2 V_n}{\partial x^2} - V_n\frac{\partial V_n}{\partial x} - \frac{1}{m_i n_n}\frac{\partial}{\partial x}(n_n k T_n) \\ + n_i(V_i - V_n)(\frac{n_i}{n_n} < \sigma_{rc} v_e > + \sigma_{cx} V_{cx} + r_{ni} + r_{in}) \\ - V_n \sigma_{wall}(\frac{n_i}{n_n} v_{Bohm} + \sqrt{\frac{7kT_n}{5m_i}})\end{aligned} \tag{2.11}$$

Second Moment

$$\begin{aligned}\frac{\partial T_i}{\partial t} = D\frac{\partial^2 V_i}{\partial x^2} - V_i\frac{\partial V_i}{\partial x} - (\gamma-1)T_i\frac{\partial V_i}{\partial x} - \frac{1}{2}n_n < \sigma_{iz} v_e > (2T_i + (\gamma-1)\phi_{iz}) \\ + n_i < \sigma_{rc} v_e > T_i + \frac{\gamma-1}{2k} n_n(\frac{1}{2} < \sigma_{iz} v_e > + \frac{1}{2}\sigma_{cx} V_{cx} + r_{in}) m_i(V_i^2 - V_n^2) \\ + (\gamma-1) n_n < \sigma_{iz} v_e > \frac{3}{4}T_n - (\gamma-1) n_i < \sigma_{rc} v_e > \frac{3}{4}T_i + \frac{\gamma-1}{k} m_i n_n \sigma_{cx} \frac{3}{8}(q_{in} - q_{ni}) \\ + \frac{1}{2}\sigma_{wall} V_{Bohm}(2T_i - \frac{\gamma-1}{k} m_i V_i^2)\end{aligned} \tag{2.12}$$

$$\begin{aligned}\frac{\partial T_n}{\partial t} = D\frac{\partial^2 V_n}{\partial x^2} - V_n\frac{\partial V_n}{\partial x} - (\gamma-1)T_n\frac{\partial V_n}{\partial x} + (\gamma-1) n_i T_n(< \sigma_{iz} v_e > - \frac{n_i}{n_n} < \sigma_{rc} v_e >) \\ + \frac{\gamma-1}{k} m_i n_i(\frac{n_i}{2n_n} < \sigma_{rc} v_e > + r_{ni})(V_i - V_n)^2 + \frac{\gamma-1}{k}\frac{1}{2} m_i n_i \sigma_{cx} V_{cx}(V_i^2 - 2V_i V_n - V_n^2) \\ - (\gamma-1) n_i < \sigma_{iz} v_e > \frac{3}{2}T_n - (\gamma-1)\frac{n_i^2}{n_n} < \sigma_{rc} v_e > \frac{3}{2}T_i + \frac{\gamma-1}{k} m_i n_i \sigma_{cx} \frac{3}{4}(q_{ni} - q_{in}) \\ + \sigma_{wall}(\frac{\gamma-1}{k}\frac{1}{2} m_i V_n^2(\frac{n_i}{n_n} V_{Bohm} + \sqrt{\frac{\gamma k T_n}{m_i}}) - \frac{n_i}{n_n} V_{Bohm} T_n)\end{aligned} \tag{2.13}$$

The derivations for this this model, including definitions for all terms and how the wall term was introduced, are detailed in Appendix A. An artificial diffusion term was also included in the numerical implementation, to add numerical stability. With all cases presented, this artificial diffusion coefficient is low enough that the model converges to an advection-dominated case as expected in the physical system. Figure 2.8 shows how the model converges when this diffusion coefficient is lowered.

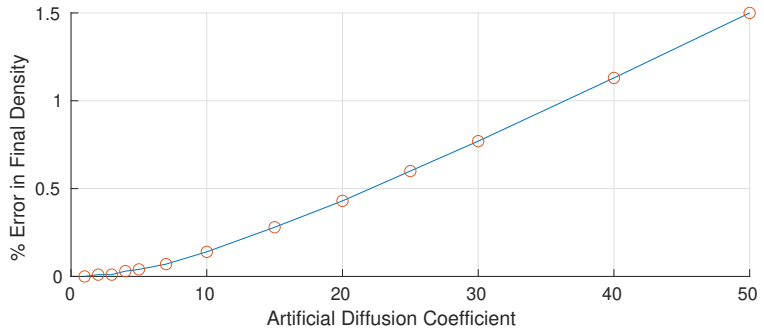

Figure 2.8: Plot illustrating convergence of model with artificial diffusion coefficient.

Adjusting the initial conditions of the model and comparing the steady-state result to experimentally determined profiles can give insight into plasma parameters that cannot be directly measured by the Langmuir probe. Initially, the model is run using a set of best guesses for the inlet plasma parameters. The initial density and temperature of the plasma comes from Langmuir probe readings, and initial velocity comes from the corresponding ion acoustic speed. A neutral density of 10^{18} m^{-3} and temperature around 1 eV are consistent with past simulation studies of the HIT-SI3 confinement volume using the PSI-Tet code [12, 11], and data from past studies using a two-photon laser induced fluorescence (TALIF) diagnostic [37, 8].

This simulation quickly converges to the profiles displayed in 2.9 for all three of the conserved quantities for both fluids. One clear difference from experimental results is that the plasma rapidly cools toward a temperature of 5 eV as it expands into the volume, which

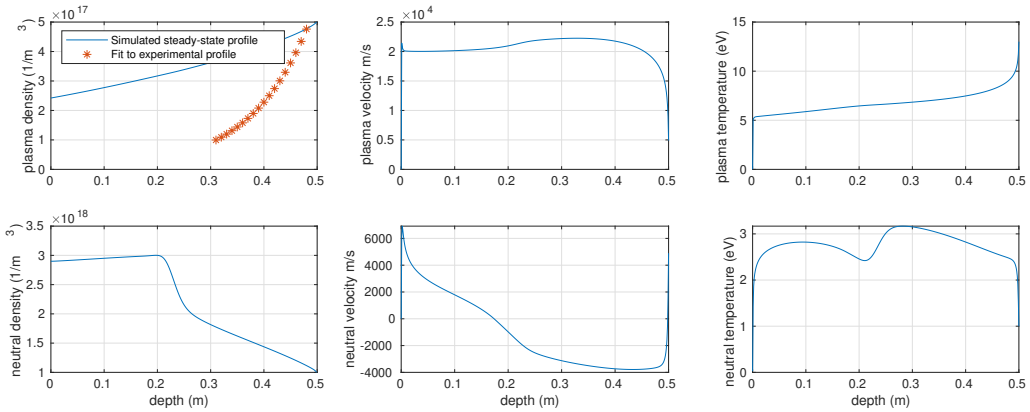

Figure 2.9: Results of converged model using initial best guess of inlet parameters: ion temperature of 13 eV; plasma density of 5×10^{17} m^{-3}; neutral temperature of 1 eV; neutral density 10^{18} m^{-3}.

is not seen in the probe data. Another thing to note is that the neutral flow is reversed for most of the length of the domain. This is because the relatively hot plasma has much higher pressure. The velocity it converges to is much higher than the initial (sonic) velocity, and the resulting strong ion transport down the length of the domain means there is a volume source of neutrals, from charge-exchange and wall recycling, which overwhelms the inlet source term.

The density profile the simulation converges to is far from that observed by the probe. They are both an exponential decay, dominated by wall losses, but the simulated profile decays much slower than the experimental. Since this is a 1D model where wall recycling is assumed to be uniform, some significant difference in the trends is expected. To get an idea as to just how large the deviation is, another set of simulations was run, enhancing the flux to the wall by a constant factor. As seen in figure 2.10, the flux needs to be enhanced by a little under a factor of eight to match the experimental profile. This is on the high end of the expected range of error for a model like this, indicating that our assumptions about the inlet parameters may be off.

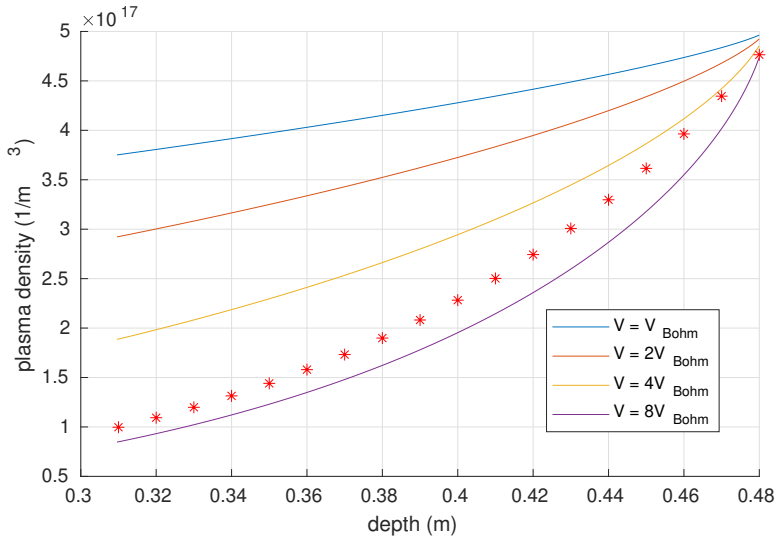

Figure 2.10: Results of several converged models with plasma wall losses enhanced by several constants.

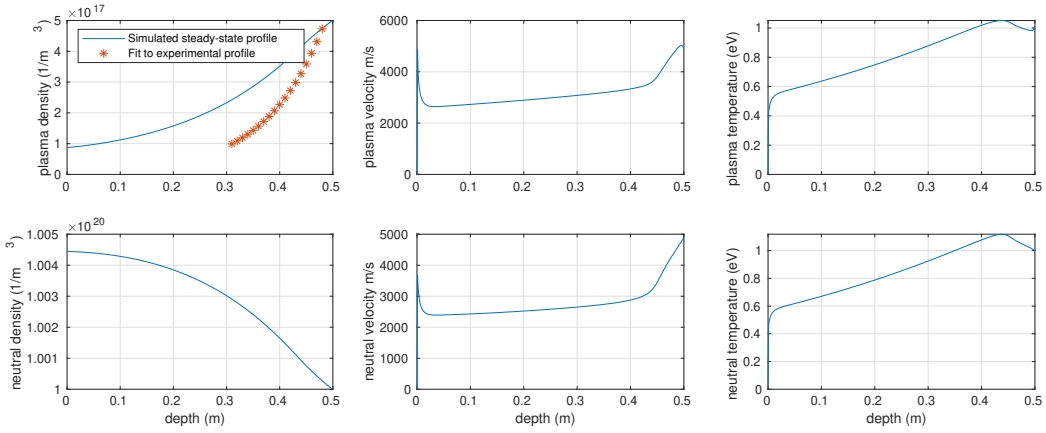

Figure 2.11: Results of converged model with plasma temperature raised to 30 eV.

As seen in figure 2.11, Raising the plasma temperature at the inlet does make the simulation closer to experimental results in some ways, and farther away in others. The temperature profile appears to follow the same dynamics as in the lower temperature case, just at a higher

absolute level. However, the density falloff is even slower than the lower temperature case, due to higher pressure and higher velocity limiting the time that the plasma can interact with the walls as it flows through. Wall flux needed to be increased by an even larger factor to get a fit.

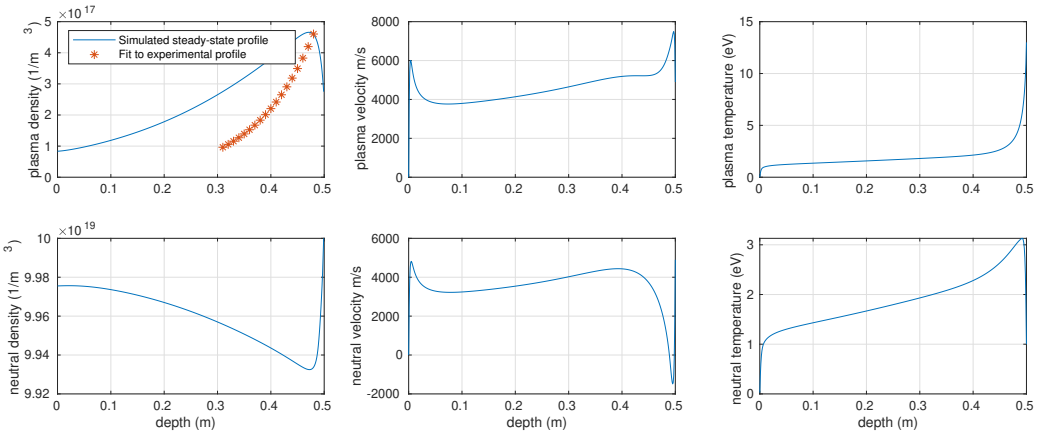

Figure 2.12: Results of converged model with neutral density raised to 10^{20} m^{-3}

The rate of plasma density falloff appears most closely related the plasma flow velocity. For higher velocity, there is less dwell time per unit length for the plasma to interact with the walls. The effect of changing the initial velocity is minimal, due to the influence of pressure terms in plasma motion. Dropping the initial plasma temperature has limited effect, because although the flow velocity is slower, the Bohm velocity is also much lower, having the opposite effect. There is, however, another way to decrease plasma velocity by changing initial conditions. As seen in figure 2.12, when the neutral density is increased without lowering the plasma temperature, ionization overwhelms the inlet source. This results in a large spike in plasma density right after the inlet, and a corresponding drop off in neutral density, which is replenished by charge exchange and wall recycling. However, this high neutral density also means that the plasma and neutral fluids equilibrate very quickly, primarily through charge-exchange. The temperatures of the two fluids match almost

immediately, and the flow velocities after less than 10 cm. The temperature profile is now very different from the experimental result, but there may be an explanation that could reconcile this. In this model, the ions and electrons are treated as a single fluid, but charge exchange only affects the ions, so it is possible in a case where energy transfer is dominated by charge exchange, the ion and electron fluids could develop a large temperature difference. However, the fast equilibration at the inlet shows that this set of starting conditions are far from any kind of equilibrium that would be expected to occur in the edge plasma. If we expect that the edge plasma already has time to expand and equilibrate before it reaches the inlet, its temperature could be much lower than the core measured by TALIF and other optical diagnostics, such as ion Doppler spectroscopy [37].

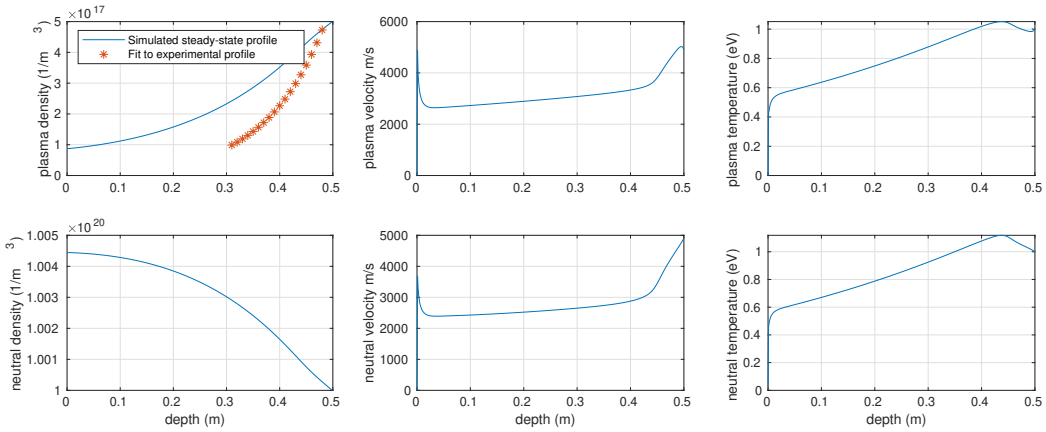

Figure 2.13: Results of converged model with neutral density raised raised to 10^{20} m^{-3} and plasma temperature decreased to 1 eV.

As seen in figure 2.13, running the simulation starting from an equilibrated case with a much cooler plasma gives an even faster density falloff, within about a factor of two of the experimentally determined profile. The initial pressure is low enough that both fluids compress and slow down after entering the domain at the sound speed. Using this set of initial parameters, plasma flux to the wall only needs to be enhanced by about a factor of 2,

to get a match to the experimental profile, putting it well within the expected range of error, so much so that a neutral density in the mid to high 10^{19} m^{-3} range is also conceivable.

2.4 Conclusions

It may seem from these results as if the experimentally determined temperature and density profiles are indicative of contradictory sets of plasma parameters. The temperature profile is best explained by high plasma temperature and low neutral density and the density profile by high neutral density and low temperature. However, there are some things that may explain this. As mentioned earlier, heat exchange between the plasma and neutrals occurs primarily through charge-exchange, which may cause the electrons to be significantly hotter than ions. Additionally, Langmuir probes are notoriously challenging to extract accurate absolute measurements from, able to be affected by a variety of types of outside interference including magnetic fields, stray RF, plasma flows, and background neutral particles. Stray field will be reduced by not eliminated by the copper louvers, and the effect of RF noise should be minimized by the steady-state nature of the triple probe [28]. Even so, having only a factor of two difference between experimentally determined and simulated profiles is reasonably close for this kind of problem, especially since the simulation in question is only 1D, and doesn't include several effects present in the true system, like that of the central rod that supports the probe, or the turbulence caused by the louvers. The high applied voltage may also be a source of error, by ionizing neutral gas between the bias tips, increasing current and effecting probe voltages in unexpected ways. Even so, these kinds of errors are more likely to produce a constant offset in the data than a strong trend with probe position, so the density profile should be more reliable than the temperature. This would indicate a cool and weakly ionized edge plasma dominated by charge-exchange, and that therefore, the passive pumping volumes not effective enough to maintain neutral density at an acceptably low level for the full duration of a HIT-SI3 discharge.

Chapter 3

PRE-IONIZATION SOURCES FOR HIT-SIU

The upgraded HIT-SIU experiment includes several features to improve plasma density control and reduce the buildup of neutrals, one of which is a set of electrodeless pre-ionization sources. These effectively go between the gas puff valves and the helicity injectors that they fuel, ionizing gas before it reaches the injectors, so they no longer will need to rely on Paschen breakdown for initial ionization. A similar plasma source was used on HIT-SI and HIT-SI3 to assist in ionization, but it was mounted to the main confinement volume and only indirectly helped to ionize the gas inside the injectors. Each of the four new sources constructed for HIT-SIU is made up of several components: a housing, an RF antenna to provide power, a solinoidal coil to apply an external magnetic field, and several machined or 3D printed structural components to hold the assembly together. Figure 3.1 shows each of these components before assembly and figure 3.2 shows how they fit together in the final assembly.

The RF antennas are powered similarly to the voltage and flux coils that power the HIT-SIU helicity injectors, using a resonant tank circuit powered by a capacitor bank and switching power amplifier. The main difference in the configuration of the two systems is that the antennas are connected in series while the injector coils are connected in parallel. In hope of increasing ionization efficiency, the antennas were assembled in the Nagoya type-III configuration with double windings, in an attempt to excite plane-polarized helicon waves [25]. The solenoidal magnetic field coils were included to provide the external field necessary for helicon waves to propagate, as well as insulating the plasma from the walls when operating as a general inductively-coupled source (ICP). These coils are powered in series by a capacitor bank, which provides a reasonable steady current during the short dura-

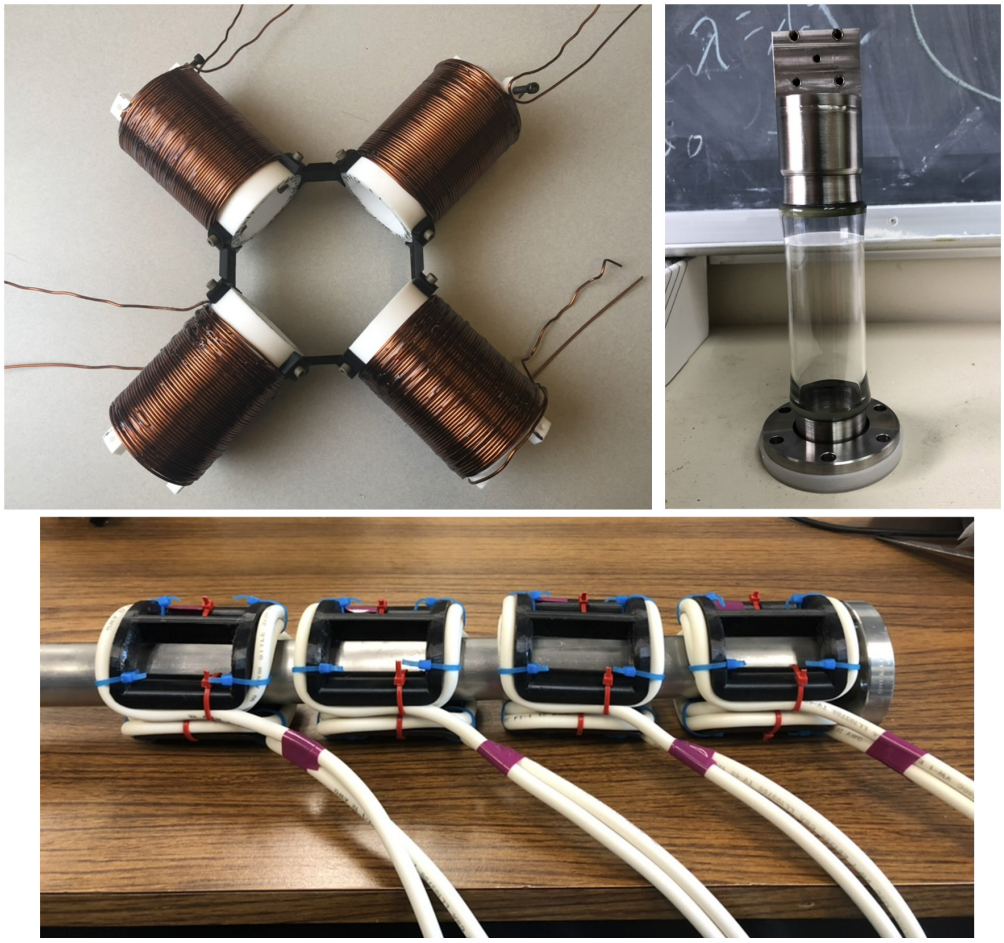

Figure 3.1: Wrapped and assembled magnet coils (top left), housing (top right), and assembled antenna coils (bottom) for all 4 sources.

tion of a spheromak discharge, as shown in figure 3.3. The power supplies are able to supply over 110 kilowatts of RF power to each of the antennas and enough current to the coils to achieve magnetic fields of up to 2.7 Tesla for the duration of a HIT-SIU discharge.

3.1 Helicon Wave Theory

Helicon waves are bounded whistler waves which are particularly efficient at coupling RF energy to a plasma. The Nagoya type-III antenna configuration effectively combines right and

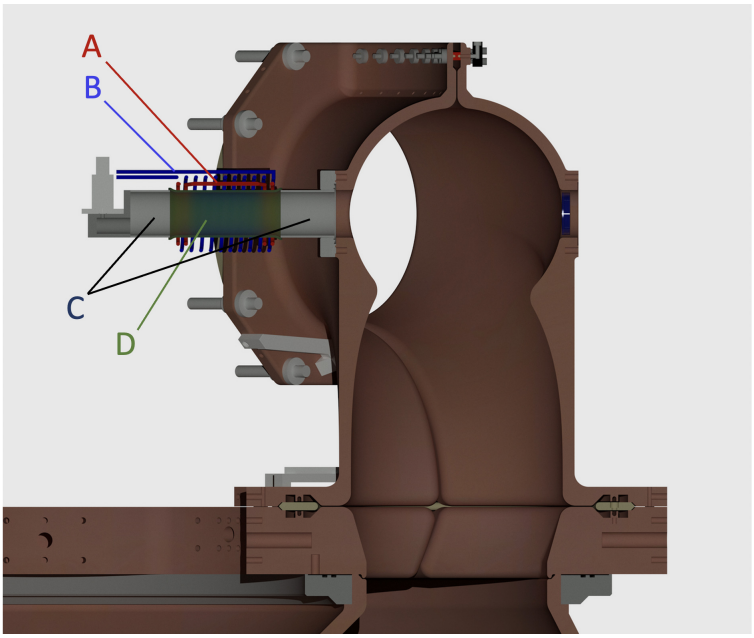

Figure 3.2: Cross-section diagram of one of the HIT-SIU injectors and pre-ionization source with A: Antenna coils, B: Magnet coils, C: Stainless Steel sections of the housing D: glass section of the housing.

left-hand circularly polarized waves, to create a plane polarized wave with nonzero parallel electric fields. These electric fields can accelerate electrons to higher velocities, improving ionization efficiency even further [25]. However, since the cables between the antenna and the power supply need to be several meters long, and are twisted to minimize stray RF, the total inductance of the system is much higher than that of the antenna alone, which prevents the circuit from reaching frequencies in the megahertz range, where helicon plasma sources typically operate [34].

To determine if helicon waves can propagate in these conditions, we need to examine the dispersion relation for these waves and compare the results to the observed parameters of the sources. Taking the determinant of the dielectric tensor for a cold, collisionless plasma gives a dispersion relation that is quadratic in the square of the perpendicular refractive

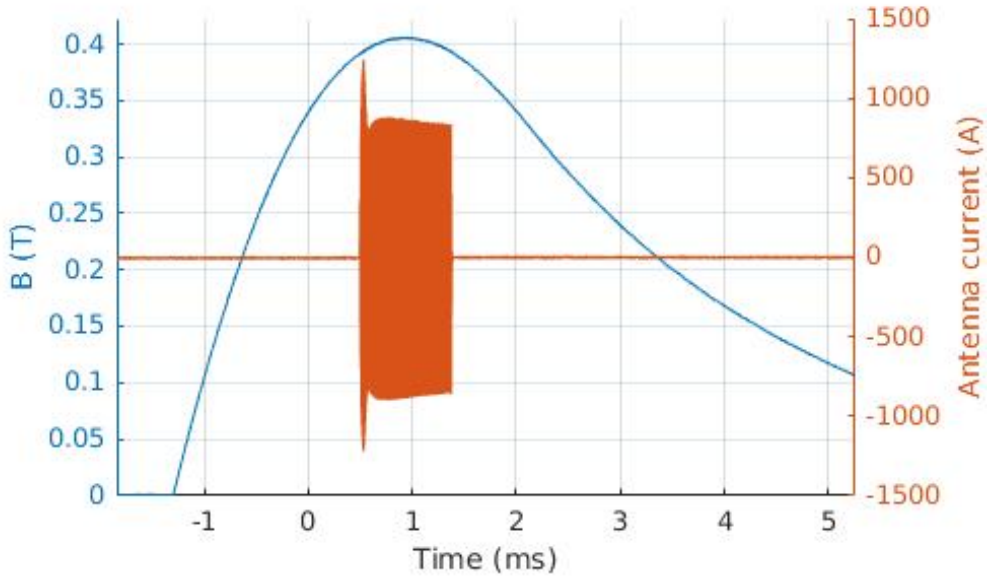

Figure 3.3: Plot of applied magnetic field (blue) and antenna current (orange) during a typical pre-ionization source discharge.

index $N_{\perp}^2$. This means that there are two real solutions for the perpendicular wave number. As detailed by Kotelnikov [20], there are two coalescence points where the wave transitions from propagating to evanescent, which can be found by setting these two solutions equal to each other. The position of these two points is dependent on the value of the parallel refractive index $N_{\parallel}^2$. And for any set of frequency and field strength, there is a critical value of $N_{\parallel}^2$ where these coalescence points overlap, so that a wave impinging on a plasma from outside never encounters a region where the helicon wave is stopped from propagating in the direction perpendicular to the magnetic field, therefore, it can penetrate the outer sheath layer of a plasma [4, 5, 20].

Figure 3.4, using the example parameters of figure 3 from Kotelnikov, shows propagating and evanescent solutions of the perpendicular index of refraction for several values of the parallel index of refraction. The top two plots, below $N_{\parallel,crit}^2$, display a gap where the propagating solutions are imaginary or zero, and only the evanescent solutions are real. This

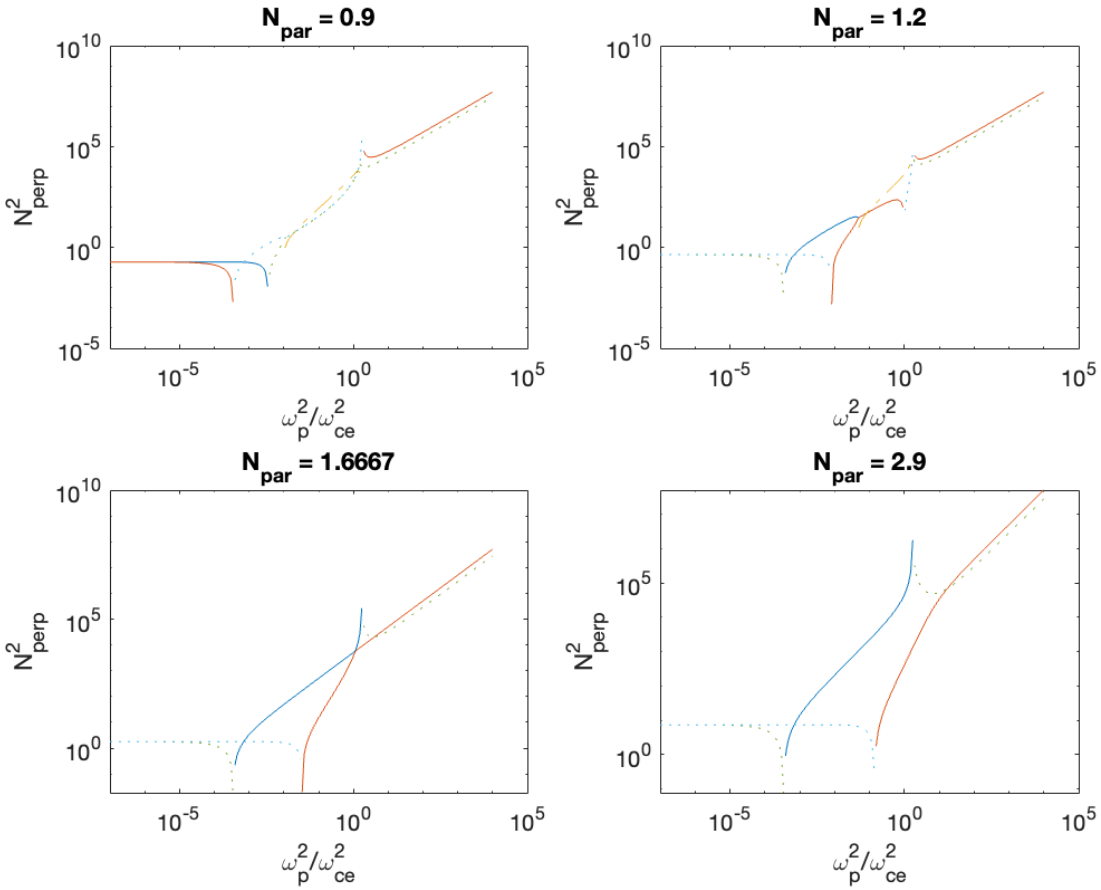

Figure 3.4: Replication of figure 3 from Kotelnikov, 2014 [20]. Dispersion diagrams at several different values of $N_{\|}$. Solid lines indicate real solutions, dashed lines indicate decaying solutions, and dotted lines indicate evanescent solutions.

gap goes away when $N_{\|}$ is raised above the critical value, as seen in the bottom two plots. For the regime where the wave frequency is less than the lower hybrid frequency for the plasma (which is the case for the present power supply and antenna configuration), the Golant-Stix criterion relates this critical index of refraction to a critical plasma density, above which, waves of this type cannot be guaranteed to propagate [20, 36]

$$N_{\parallel}^2 \geq 1 + \frac{\omega_{p,res}^2}{\omega_{ce}^2}. \tag{3.1}$$

Where the resonant plasma frequency is given by

$$\omega_{p,res}^2 = \frac{n_e e^2}{m_e \epsilon_0} = \frac{(\omega_{ce} - \omega^2)(\omega^2 - \omega_{ci})}{\omega_{ce}\omega_{ci} - \omega^2}. \tag{3.2}$$

Combining these expressions and simplifying gives an approximate density limit

$$\frac{n_e e^2}{m_e \epsilon_0} \approx \frac{\omega_{ce}}{\omega ci} k_{\parallel}^2 c^2 \tag{3.3}$$

For the conditions expected in HIT-SIU pre-ionization sources, this density limit is very low, on the order of 10^{13} m^{-3}. This is primarily due to the low frequency, which has a much stronger effect on this limiting density than field strength [20]. Typical helicon plasma sources have operating frequencies less than a factor of 20 higher, which would result in a density limit on the order of 10^{15} m^{-3} or 10^{16} m^{-3}. However, they are able to exceed this density by many orders of magnitude because they operate in a regime where operating frequency is higher than the lower hybrid frequency, so the Golant-Stix criterion is no longer valid. Instead, the Shamrai-Taranov relation is used, resulting in a different expression for the density limit that allows these sources to continue to heat plasmas with density up to 10^{20} m^{-3}, and even higher, theoretically [20, 34].

Figure 3.5, a plot analogous to a dispersion relation, shows that even with the most favorable parameters achievable, there is no case in which a real solution for $N_{\perp}^2$ exists for the entire density range from vacuum all the way to the high density plasma being heated. The plots with $N_{\parallel}^2 < 1$ indicate cases where the vacuum wave is able to propagate, but at some point in the plasma sheath as density ramps up, the wave becomes evanescent and cannot penetrate [20]. The solutions with $N_{\parallel}^2 \geq 1$ indicate solutions where the wave can propagate in some manner for the whole width of the sheath, but not in vacuum [20]. This analysis suggests that helicon waves will not be present in the HIT-SIU pre-ionization sources, but is not entirely conclusive. It is still possible that these waves could tunnel through the

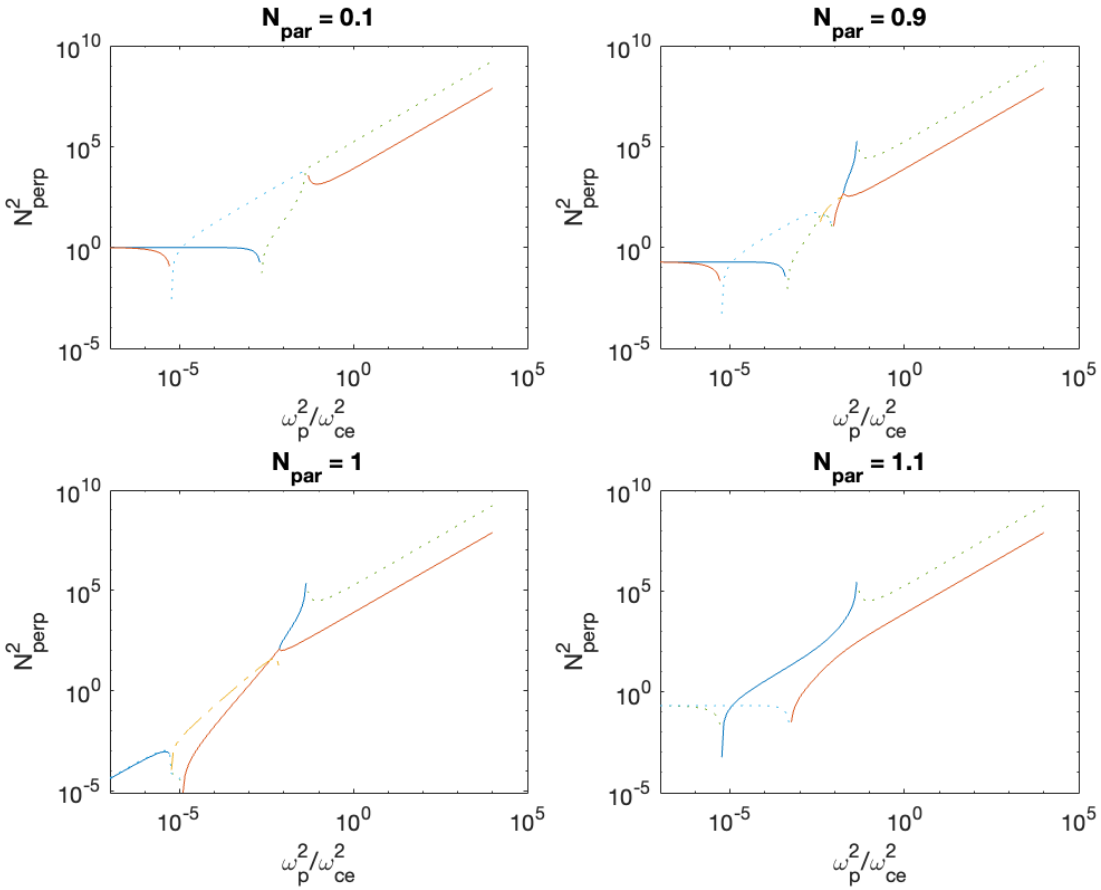

Figure 3.5: Dispersion diagrams at several different values of $N_{\|}$, using an estimate of the lowest achievable magnetic field for the HIT-SIU pre-ionization sources, to get as close as possible to the lower hybrid frequency. Solid lines indicate real solutions, dashed lines indicate decaying solutions, and dotted lines indicate evanescent solutions.

evanescent region of the sheath, which is very thin. The physical system also does not satisfy the assumptions that go into the initial dispersion relation. These plasma sources routinely achieve temperatures of 10-20 eV and densities up to 10^{20} m^{-3}, meaning they are far from being either cold nor collisionless.

Since this design is unlikely to excite helicon waves within the plasma, it must act as a

more conventional electrodeless plasma source, inductively coupling energy to the plasma. For inductively-coupled plasma (ICP) sources, a magnetic field applied externally is not expected to enhance wave-particle energy coupling, but it will still help insulate the plasma from the walls of the source, and direct the flow outward into the volume of the helicity injection manifold [40].

3.2 Plasma Source Diagnostics

The next objective was to characterize the performance of the sources by adjusting the applied magnetic field strength and the pressure on the gas puff valves, in order to inform a set of standard operating parameters for HIT-SIU spheromak discharges. Four diagnostics were used in this study: 1) the triple Langmuir probe described in section 2.2, 2) an ion Doppler spectroscopy (IDS) diagnostic, 3) Rogowski coils measuring current through the antenna and magnet coils, and 4) high speed cameras to observe plasma breakdown and look for signs of surface arcs or other plasma-material interactions that could be problematic for HIT-SIU operation. The probe, IDS optics, and two cameras were all mounted on separate sources, so they could be used simultaneously. Additionally, during some tests, one of the cameras was replaced with a photomultiplier tube to better quantify the exact time of plasma breakdown. Figure 3.6 shows how the sources are laid out, mounted to the inboard side of the helicity injection manifold, with a diagnostic port for each on the outboard side.

Once the plasma sources were installed, the Langmuir probe from the previous study was installed through an outboard port on the helicity injection manifold opposite one of the sources. In this configuration, it had a traverse distance of 25 cm, enough to go all the way from a position with the tips just inside the plasma source (figure 3.7), to a position where the probe tips were recessed inside the port, so they did not protrude into the injector volume.

Since the probe needs to operate in an environment with much stronger and higher frequency RF than it was exposed to in previous studies, it was an open question whether its reading would remain valid. Caneses and Blackwell derive a criterion for RF-compensation

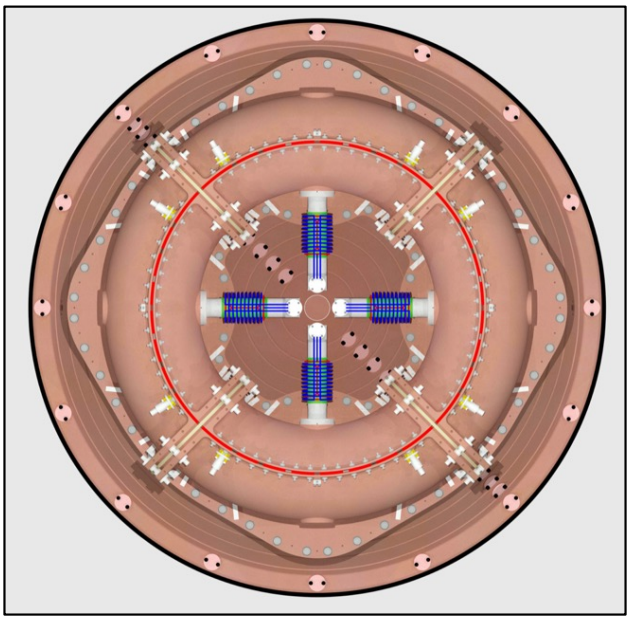

Figure 3.6: Diagram showing a top view of the helicity injection manifold with the plasma sources installed on the inboard side (magnet coils in blue). Diagnostic ports are opposite, on the outboard side.

extendable to a wide variety of plasma probes, based on RF frequency, electron flux, and probe capacitance. If this criteria is met, the probe does not have any significant RF rectification effect, and is therefore self-compensating [3]. Our probe satisfies this criterion by several orders of magnitude. Another factor that may bias the probe readings is the applied magnetic field. Since the probe is generally in the same direction as the applied magnetic field, and the ramp time for the magnetic field is much longer than any other characteristic time in the system, the primary way it is expected to affect the probe is by restricting electron motion in the cross-field direction, decreasing the effective collection area [40]. As mentioned in 2.2, a constant factor applied to the current on all of the probes that make up a triple probe will cancel out in the calculation of electron temperature, but does factor into the calculation of electron density. With our probe geometry, the apparent electron density may decrease by as much as a factor of 3 when strongly magnetized, but the temperature

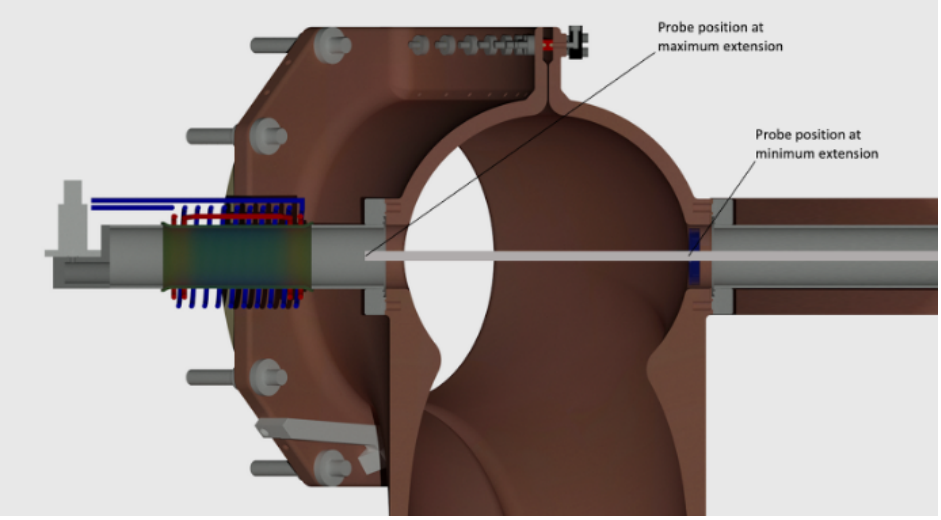

Figure 3.7: Cross-section diagram of one of the HIT-SIU injectors and pre-ionization source, illustrating the traverse length of the triple probe.

reading should be unaffected [28].

Just like for the pumping volumes, the first experimental objective with the triple probe was to estimate the plasma flow velocity at the probe tip, determine if a calibration factor needs to be applied for density measurements, and if so, determine what that factor should be. This was done in the same manner as in section 2.2. For an initial standard set of operating parameters for the plasma source, figure 3.8 shows the flow velocity is much lower than an estimate of the ion acoustic velocity made from the probe's electron temperature reading ($\approx 2 \times 10^4$ m/s), indicating that a correction factor for the density is not needed for this regime.

The relatively low flow velocity may be due to ion-neutral interactions slowing down the plasma component of the plume, which is otherwise expanding into a vacuum. The plasma-neutral transport model presented in the previous chapter shows that this regime of dense, warm plasma is often dominated by charge-exchange, suggesting that there is still a large neutral component to the plume.

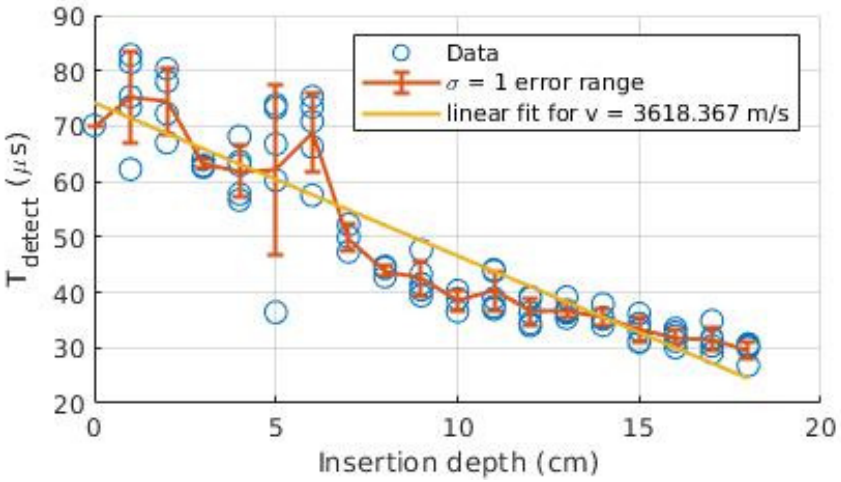

Figure 3.8: Probe position vs time for the probe to detect plasma relative to breakdown, with linear fit indicating an inferred flow velocity.

Because of the uncertainties involved when using a Langmuir probe alone, an ion Doppler spectroscopy diagnostic was also employed, so that gross errors or biases with either diagnostic could be identified. The method is similar to that described by Hossack [14], but with slightly different hardware. The lens and fiber optic bundle leading to the spectrometer was mounted on a port similar to that used by the Langmuir probe, to direct its field of view down the length of the plasma source as shown in figure 3.9.

The spectrometer in question is a Ritsu Ohyo Kogaku MC-100N grating monochromator with a focal ratio of 8.5 and a focal length of 1 meter. The detector was a second Phantom high speed camera, similar to those used to monitor plasma-material interactions. This system provides good time resolution, but has lower sensitivity compared to systems using photomultiplier tubes or a purpose-built CCD detector. For this reason, The IDS diagnostic was not able to detect a significant signal from helium or deuterium ions, but it was able to resolve line spectra from neutral helium. This suggests that similar to the pumping volumes, there may be strong ion-neutral coupling in this system which keeps the ions significantly cooler than the electrons. This also means that some data had to be collected using helium

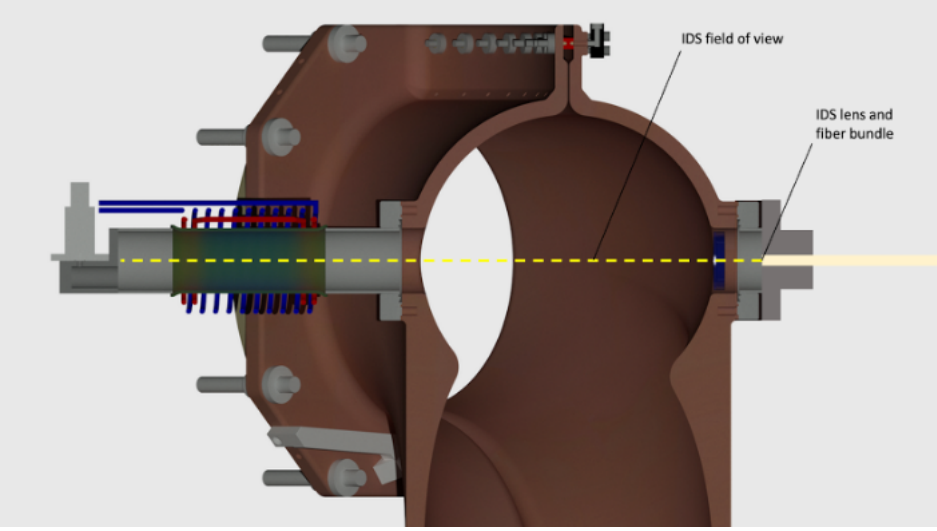

Figure 3.9: Cross-section diagram of one of the HIT-SIU injectors and pre-ionization source, illustrating mounting and field of view of IDS system.

and deuterium, to have one set of data allowing diagnostics to be verified with each other. We were not able to obtain an absolute calibration for this particular implementation of the IDS diagnostic, but the relative trends are still of some limited value, given that the rate of the excitation process corresponding to this signal should be proportional to neutral density, electron density, and an exponential term containing electron temperature [28]. Since the Langmuir probe is able to measure two of these three properties, and the third, neutral density is expected to be strongly related to the puff valve pressure, it can provide some additional insight into the causes of certain trends.

In order to measure the absorbed power from the antennas, it would be ideal to measure both the voltage across and the current through the antennas. However, given the design, we only have access to a current measurement, from integrating the signal from the Rogowski coil. However, we can still infer the absorbed power from a circuit model by finding a set of circuit parameters that produce a matching current waveform. When no plasma is present, the power should be exclusively reactive ($L >> R$), since the line resistance is very low (less

than an Ohm). Any significant resistive load introduced by the plasma will shift the phase of the current signal, indicating an active component to the power. Comparing the phase of the antenna current signal from shots with and without plasma gives a phase difference, the cotangent of which gives the ratio of active to reactive power.

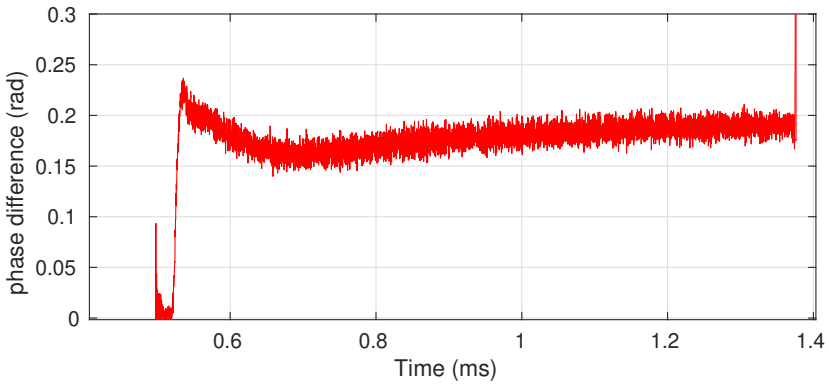

Figure 3.10: Example of the phase difference between a vacuum and plasma discharge. Breakdown occurs at approximately 0.52 milliseconds, and the quiescent period begins around 0.8 to 1 ms.

As seen in figure 3.10, there is very little phase difference between vacuum and plasma shots prior to breakdown, then the current phase pulls ahead when breakdown is achieved and the plasma is at its peak power absorption. Later on in the discharge, the gap between the two phases closes somewhat as the plasma becomes quiescent. This phase difference during the quiescent period, along with the current amplitude at the same point, are the parameters that the aforementioned circuit model needs to match. The circuit is modeled as a single transformer driven by a square wave, with the four series antennas represented as a single load with unknown resistance and inductance. This circuit was simulated using a python code originally designed to model the helicity injector circuits. Running many simulations using different values of the unknown parameters R_p, L_p, and the transformer coupling coefficient M provided a database to match the experimental current waveform

parameters to. What is remarkable about these results is that while there is a substantial range in the waveform parameters from the experimental data, the power in the simulated circuits they most closely match is very similar, between 111 and 115 kilowatts. This indicates that the resistive component of the load is not strongly affected by changes in the plasma parameters.

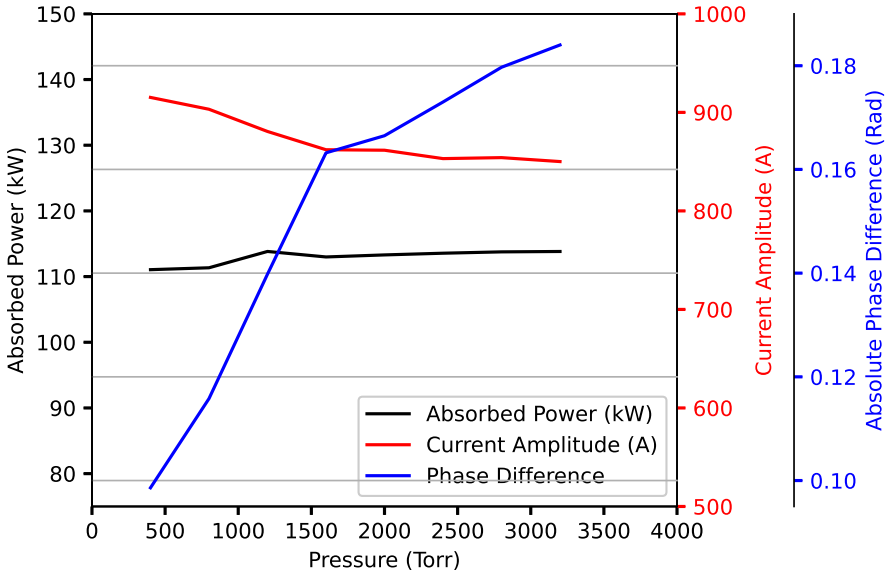

Figure 3.11: Variance in circuit parameters when changing puff valve pressure. Note that the lower bound of the scale for each is approximately 50% of the maximum value, to show the relative variation in each.

3.3 Plasma Source Characterization

The initial Langmuir probe study intended to find a rough flow velocity to be used for calibration also provided temperature and density results, shown in figure 3.12, although for density no correction for the magnetic field is applied, so the density inside the mouth of the source may be up to 3 times higher than indicated, but the exact magnitude or falloff rate

of this factor could not be determined using the available diagnostics.

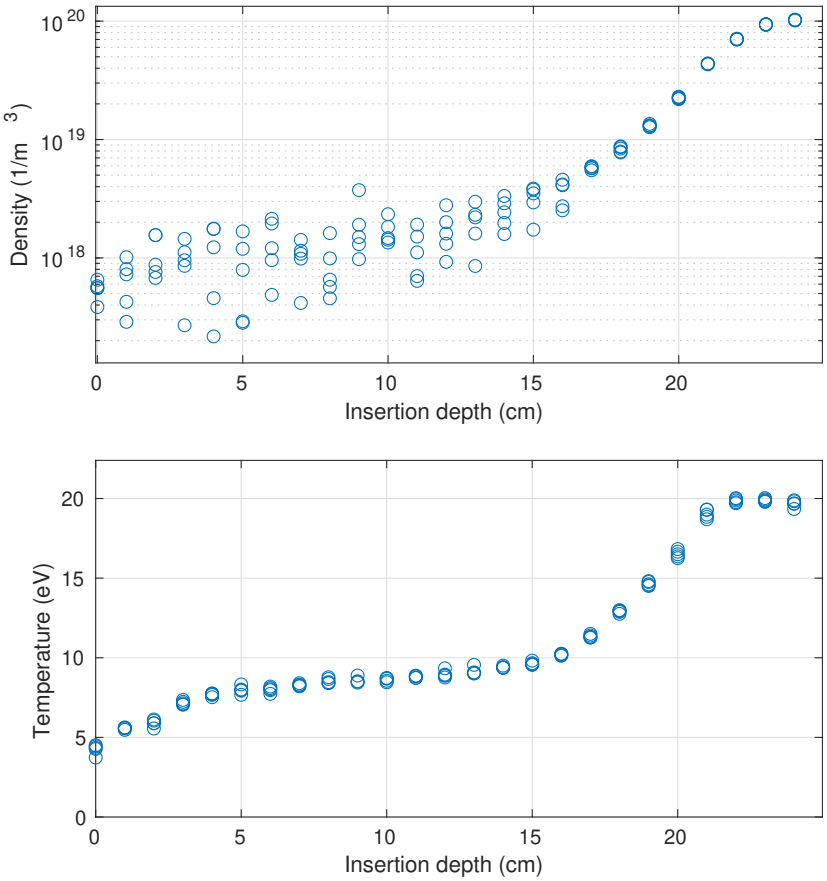

Figure 3.12: Electron density (top) and temperature (bottom), as measured by a triple Langmuir probe, at multiple points inside the helicity injection manifold.

Plasma density and temperature are very uniform, and drop off smoothly outside the source, as expected in a quasi-adiabatic system, although the adiabaticity of the system could not be estimated due to the lack of 2D information on the shape of the plume. The plasma density and temperature inside the source are both significantly higher than what are typically achievable in helicon plasma sources, which is likely due to the high power density of the system and high initial neutral density introduced by the puff valves.

The next task was to characterize how the performance of the source changes when

the applied magnetic field strength is varied. This data was collected using helium as the working gas, in order to have simultaneous probe and IDS data. There should be little difference in how D_2^+ and He^+ ions react to magnetic fields, because their charge-to-mass ratio is nearly identical. A high puff pressure of 3000 Torr was used, frequently used by the HIT-SI3 gas injection system. Figure 3.13 displays the measured electron density and electron temperature over a wide range of field strengths, with a focus on the low field region since that is where any potential helicon wave activity, as well as resonances like the ion cyclotron resonance would be expected to be. A known property of helicon plasmas is that when sufficient power is present, density tends to increase linearly with applied magnetic field [9]. However, figure 3.13 shows that in the region of low field, where helicon waves would be expected, if they were present at all, the density curve appears to be flattening out. This indicates no strong transition from zero field to low field. There are the few outlier points present, but they don't appear tied to any resonances or other expected phenomena that might cause a discontinuity in antenna-plasma coupling. This is supported by the circuit modeling, which suggests the antenna power is uniform across this range of magnetic field. However, an unexpected feature is the density, as measured by the probe, increases by nearly a factor of 8 as field strength is increased. If the magnetic field is causing the probe to experience strongly anisotropic electron flux, the true factor could be as high as 24.

In general, applying an external magnetic field has been found to decrease power absorption in ICP sources, since it restricts electron motion in the perpendicular direction [40]. This same effect should be decreasing the probe current and making the density look lower than it actually is. Electron temperature, which is directly related to the ionization rate, does not increase. In fact, it appears to go down slightly, so the higher density at high field would not seem to be related to an increase in the absorbed power or energy confinement of the source region. This could be due to the magnetic field confining the plasma radially, resulting in density buildup at the center, where the probe tips are. However, that wouldn't necessarily explain the drop in temperature. Electron temperature has been observed to fall with increased axial field, but this was accompanied by lower density due to less efficient

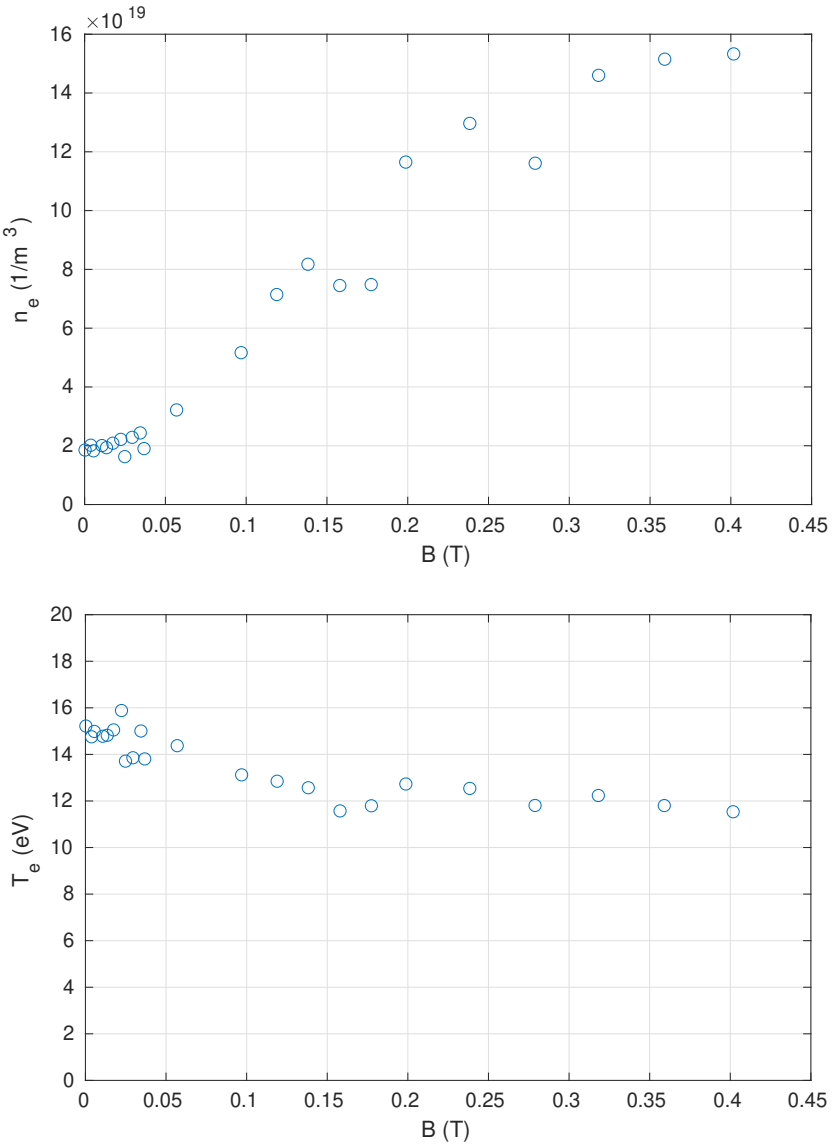

Figure 3.13: Measured electron density (top) and temperature (bottom) from triple probe vs. applied magnetic field.

ionization. Given that the peak magnetic field in this study is far higher than what have typically been used in studies of ICP sources, it is possible that the confining effect from the axial field is so strong that the probe is seeing a much higher density despite a lower overall

ionization rate.

The IDS data indicates significant ion-neutral coupling. Neutral temperature, at least near the centerline where the lens is focused, is around 1 eV, meaning that interactions with the plasma bring it up to a significant fraction of the plasma temperature. It is likely that this coupling is primarily caused by charge exchange with the ions, making the ion temperature significantly lower than the electron temperature. Neutral temperature may be increasing somewhat with field strength, but it is hard to tell for sure given the spread of the data. IDS signal intensity decreases with field strength, broadly similar to electron temperature. If the exponential dependence on electron temperature is strong, this could be from the small decrease in temperature overwhelming the effect of higher density. Alternatively, it could indicate a higher ionization fraction, if by raising the electron density, at least locally, the axial field is bringing the plasma away from the 1:1 ratio of electrons to neutrals which will produce the greatest ionization rate, if the total quantity of nuclei is constant.

Based on the Langmuir probe data, operation at high magnetic field appears to significantly enhance electron flux at the source mouth, which may make it advantageous for HIT-SIU spheromak operations. However, it was also observed to have some negative effects. At lower pressure and high magnetic field, breakdown becomes unreliable, likely due to the magnetic field restricting electron motion [1]. To quantify this and set parameters for further characterization of puff valve pressure, another set of data was collected, picking several values of pressure and sweeping magnetic field for each, to find the threshold that reliable breakdown was achieved. This was measured using a collimating lens fiber-optically coupled to a photomultiplier tube mounted to one of the ports opposite the sources. The results from this study are shown in figure 3.15.

The gas system could not reliably supply pressures below 400 Torr, so a magnetic field of less than 0.35 T is sufficient to allow reliable breakdown at any accessible pressure. Even at very high field, when the electron density appears to level off, pressures much lower than the 3000 Torr used most often on HIT-SI and HIT-SI3 are still accessible. Even so, scans over puff pressure from then on were conducted at very low magnetic field ($\approx$ 0.02 T), to

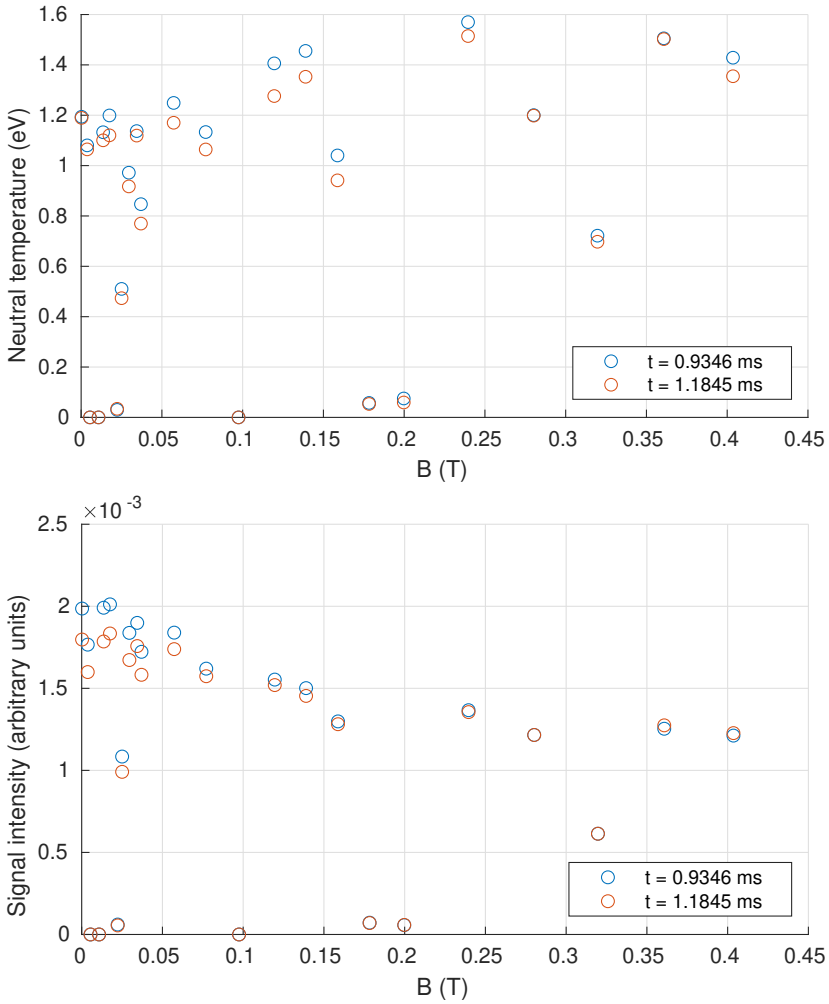

Figure 3.14: Neutral temperature (top) and Signal intensity (bottom) from IDS vs applied magnetic field. Blue and orange points indicate data captured at two different points in time.

minimize any effects that could be throwing off Langmuir probe readings.

For deuterium, the trends in density and temperature, shown in figure 3.16, are fairly smooth across all values of the puff valve pressure. In this study the electron density is expected to be more accurate than in the previous study, due to the low magnetic field. Density appears to fall off smoothly with pressure, making a wide range of plasma densities

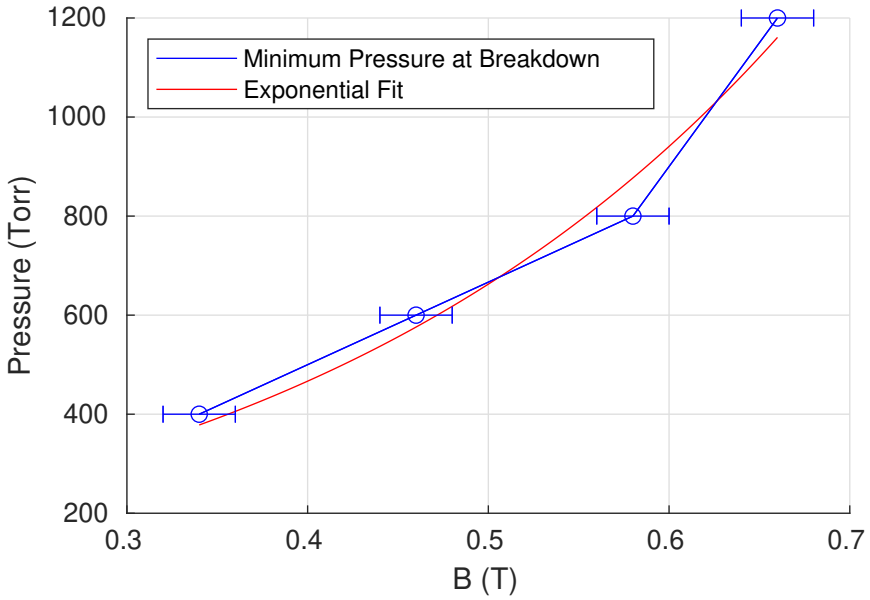

Figure 3.15: Minimum puff valve pressure to achieve breakdown with several values of magnetic field strength.

accessible. Assuming that raising the applied field has a similar effect on density with deuterium as with helium, this means that a full two orders of magnitude range should be accessible by tuning these two parameters. The electron temperature at higher pressures is much lower than was seen in any of the previous helium discharges, but it does rise as pressure decreases. This could be due to weaker electron-neutral coupling, or just fewer electrons to absorb the incoming RF power. Helium behaves differently as the working gas, as shown in figure 3.17. Presumably due to its higher ionization potential, helium gives a lower electron density and much higher temperature, indicating weaker electron-neutral coupling. The accessible range of temperature and density is also significantly lower than it is with deuterium, although the trends are still smooth.

With more data per points for each set of experimental parameters, the IDS data, presented in figure 3.18 show clearer trends than in the magnetic field study. Neutral tempera-

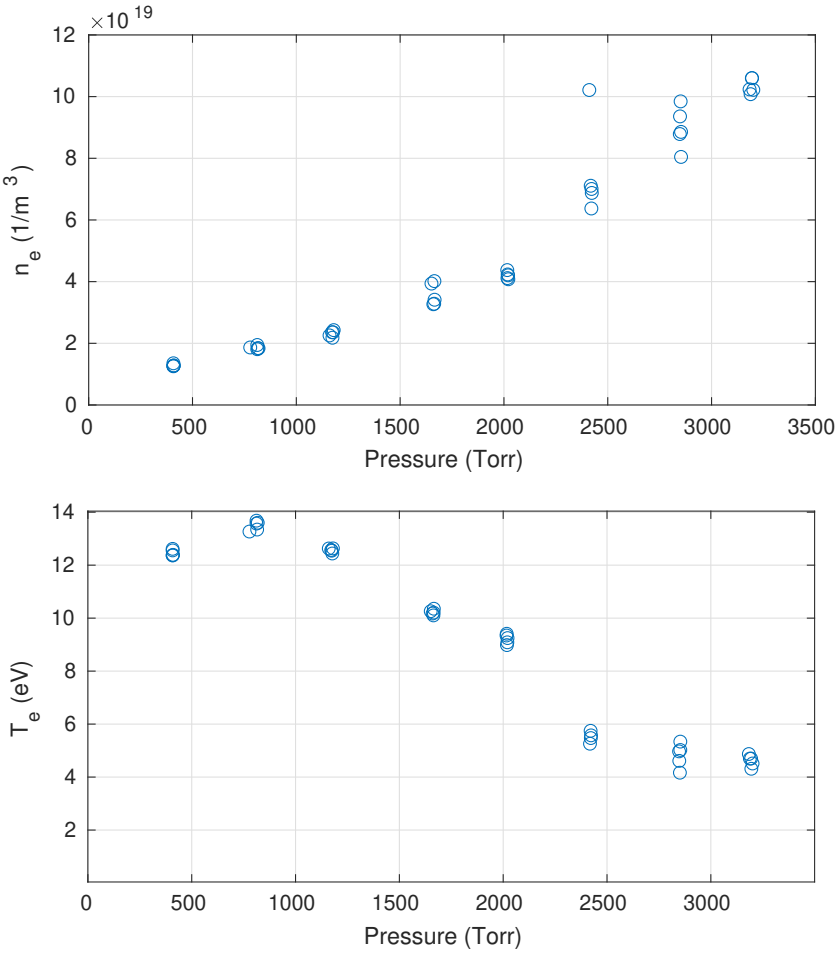

Figure 3.16: Measured electron density (top) and temperature (bottom) from triple probe vs. deuterium pressure applied to puff valve.

ture is roughly constant at higher pressures, but dips down at low pressure. This is somewhat counterintuitive, since the electron temperature and ionization fraction are higher, but as the energy transport equations in appendix A show, the reaction terms in the neutral energy equation are proportional to either the absolute neutral or electron density, so lower overall density. Similar to the previous results, the IDS signal intensity also suggests either a strong dependence on electron temperature, or an ionization fraction that is moving away from 0.5. However, one of these two possibilities can be eliminated by looking at both sets of data

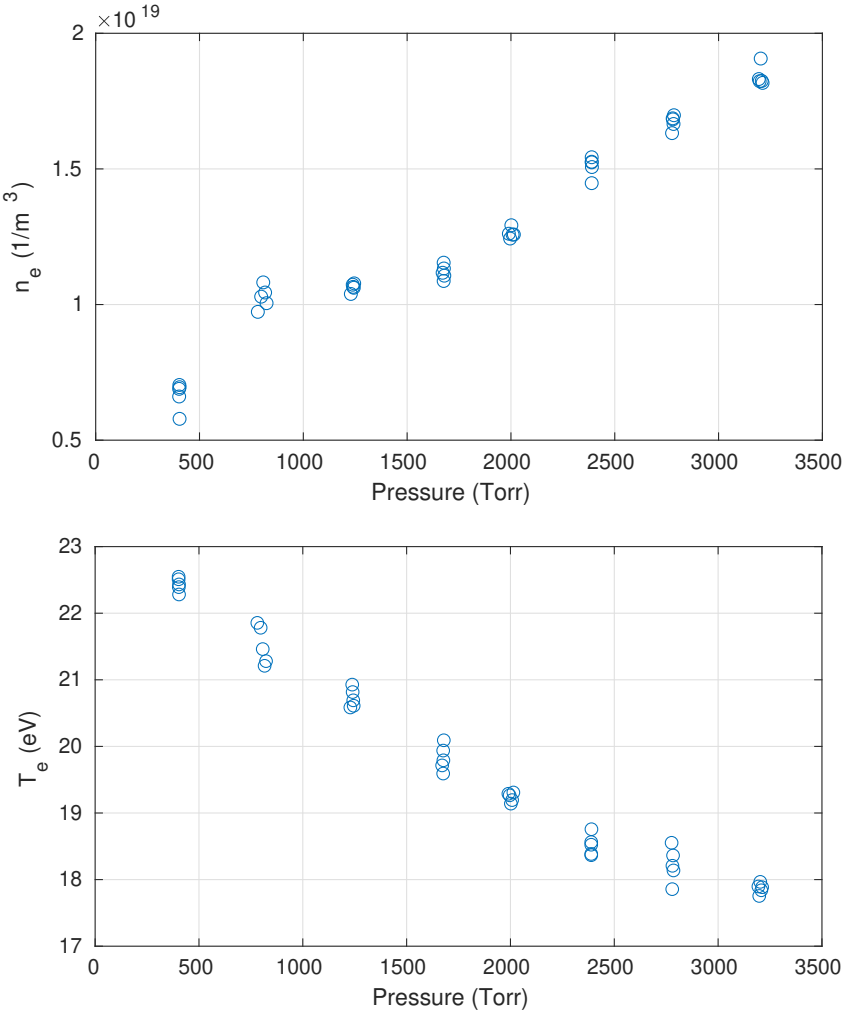

Figure 3.17: Measured electron density (top) and temperature (bottom) from triple probe vs. pressure applied to puff valve for He discharges.

relative to each other. Given that the pressure scan spans a much wider range of electron temperature than the magnetic field scan, if the explanation based on strong temperature dependence were true, raising pressure should decrease IDS intensity by a proportionally larger factor than raising magnetic field. However, the data shows the opposite, that there is a slightly larger proportional change when varying magnetic field. This may suggest that ionization fraction plays just as much, if not an even greater role than electron temperature,

but analysis this is fairly speculative. It is also possible that the magnetic field is having an unexpected effect of the probe readings that makes density appear higher than it really it. A measurement error like this would also explain disagreement with past studies on ICP sources [40].

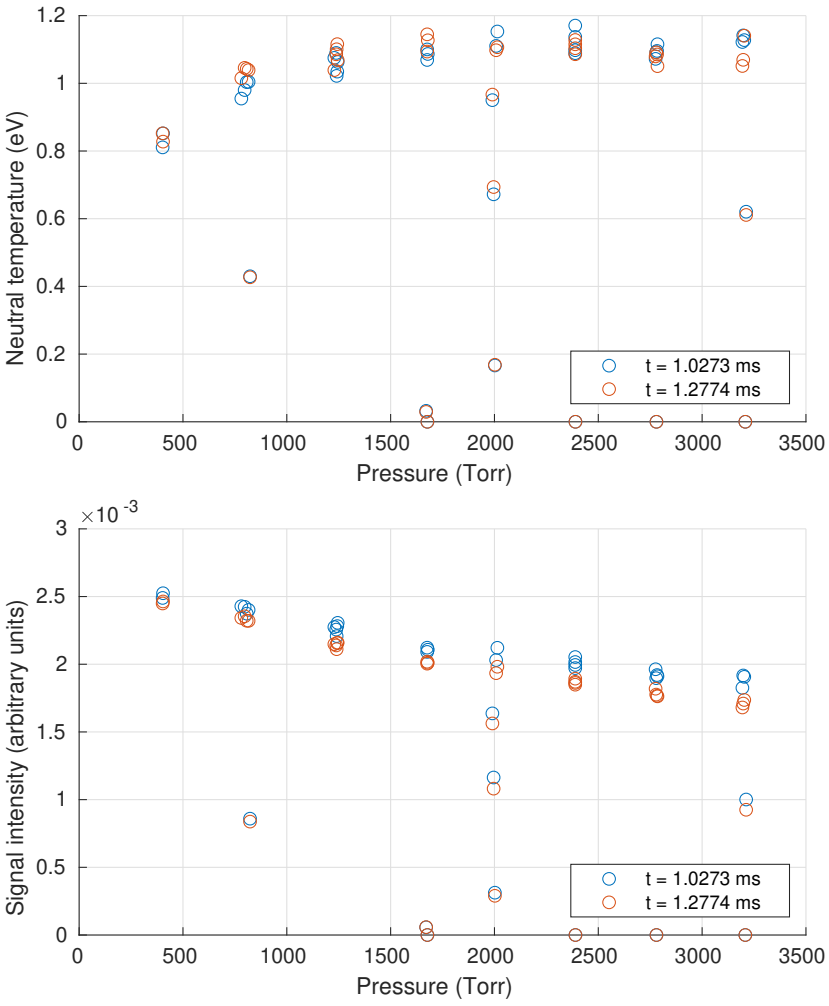

Figure 3.18: Neutral temperature (top) and Signal intensity (bottom) from IDS vs. pressure applied to puff valve for He discharges.

3.4 Conclusions

A set of electrodeless plasma sources were assembled for HIT-SIU to preionize gas flowing into the helicity injectors. Although they were assembled with a antenna design capable of exciting helicon waves, theory and experimental results suggests that they are unlikely to generate helicon waves, due to the properties of the power supply. Langmuir probe and IDS diagnostics were used to characterize them over a range of applied magnetic field and a parameter which is a proxy of neutral fueling rate. The sources have been determined to produce a wide range of plasma densities, and although there are signs of significant ion-neutral coupling, they may be able to able to produce a high ionization fraction > 0.5 in certain operating regimes.

Chapter 4

EFFECT OF SOURCE OPERATION ON HIT-SIU PERFORMANCE

One of the most important parameters to measure in spheromaks produced in the HIT-SI family of experiments is the current drive parameter j/n. This not only indicates how effective the injector fields are at driving current, but is also related to the power density of Ohmic heating [18]. The Greenwald limit [10] is a loose empirical scaling law, relating the maximum operating density for a wide variety of toroidal confinement configurations to total current and minor radius. Tokamaks, stellarators, and reversed-field pinches tend to encounter instabilities that significantly degrade performance and/or terminate discharges near or above this limit, typically driven by radiative cooling. Spheromaks have not been studied enough at high power to confirm that they follow this limit in the same way, but optimized operating parameters from the CTX and SSPX experiments do tend to follow the same general trend [10]. After the pre-ionization sources installed on HIT-SIU were characterized and shown to consistently produce a wide range of plasma densities, the next step was to use them to fuel spheromak discharges and assess how this new fueling method affects j/n evolution. In HIT-SIU, two diagnostics are used to measure this parameter, an array of surface-mounted magnetic probes to measure toroidal current and a multi-chord, two-color interferometer to measure line-integrated plasma density [16].

The magnetic field probes that form the surface probe array are embedded in the walls of the main confinement volume. As shown in figure 4.1, they are arranged in four sets, creating approximate Amperian loops around the poloidal cross-section of the plasma, allowing them to measure the total toroidal plasma current. In previous work on HIT-SI and HIT-SI3, a single-chord heterodyne interferometer was used to measure electron density. It was made up

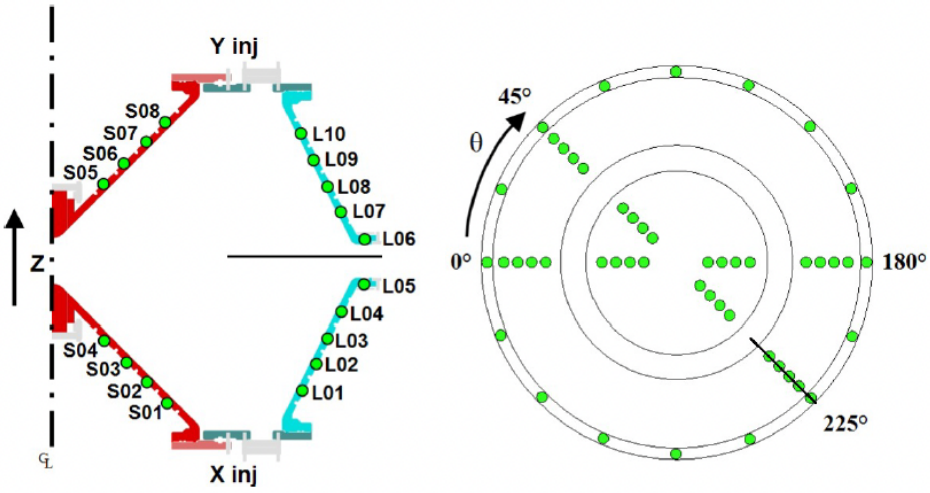

Figure 4.1: Illustration of the locations of embedded magnetic probes in HIT-SIU confinement chamber. Left: toroidal cross-section, Right: vertical cross-section.

of a difluoromethane laser and a CO_2 laser arranged in the Martin-Puplett configuration [30]. However, during the final campaign of HIT-SI3 and continuing to HIT-SIU, a multi-chord interferometer was implemented, using a CO_2 laser as the primary and a He-Ne laser for vibration compensation, which is detailed by Hossack in a paper which has been accepted for publication in Review of Scientific Instruments. The primary improvement over the previous system is the additional chords intended to construct a density profile, but it is also able to resolve a wider range of densities than the previous system and do so with much lower error.

4.1 Low Power Results

Spheromak operations began on HIT-SIU, after the helicity injector circuits were fully assembled and tuned. The Langmuir probe from the previous study was removed, to avoid possible arcing on the probe tips due to the large electric fields induced inside the helicity injectors by the voltage coils, although the IDS spectrometer was retained. In addition to

the plasma sources described in chapter 3, a set of four gas puff valves were also installed as part of the helicity injection manifold, to enable easy switching between the two fueling types, or to use both at once. The original plasma source from HIT-SI3 was also retained at its prior location attached to the confinement volume opposite the injector manifold. Operations using the new pre-ionization sources began at low power, so that any issues or defects that could pose a problem for high-power operation would be detected early.

Figure 4.2 displays toroidal current and line-integrated density for sets of two discharges using both fueling types at high pressure (3200 Torr) with deuterium as the working gas. The field strength applied to the plasma sources was kept low, to avoid any possible interference with the injector fields. As figure 4.2 shows, the immediately obvious difference between the two sets is that the discharges with plasma source fueling breakdown much earlier, and since both do so nearly simultaneously, this suggests that they are able to achieve breakdown more reliably than puff valve fueling, even at higher pressures. The density during the quiescent period is broadly similar in both sets, but there is a notable difference: with puff valve fueling, density steadily creeps up over time after breakdown. This is a behavior commonly seen on HIT-SI and HIT-SI3 discharges, likely caused by neutral gas buildup in the confinement volume. Using plasma source fueling, HIT-SIU still displays some of this creep, but to a much lesser extent. Slightly higher current and similar density results in higher j/n for plasma source fueling. Since these are low-power discharges, it is expected that they will have density above the Greenwald limit (j/n below the dotted line in figure 4.2). What matters more for these conditions is consistency. j/n is not clearly more consistent with plasma source fueling, since current and density are uneven in both cases, and if anything, a little bit more uneven with plasma source fueling. Plasma source fueling does result in clearly better performance earlier in time, with toroidal current that is both higher and more consistant between the two discharges that make up the set. Better results may be achieved by operating at lower pressure, reducing neutral gas buildup even further, but this initial data does appear promising.

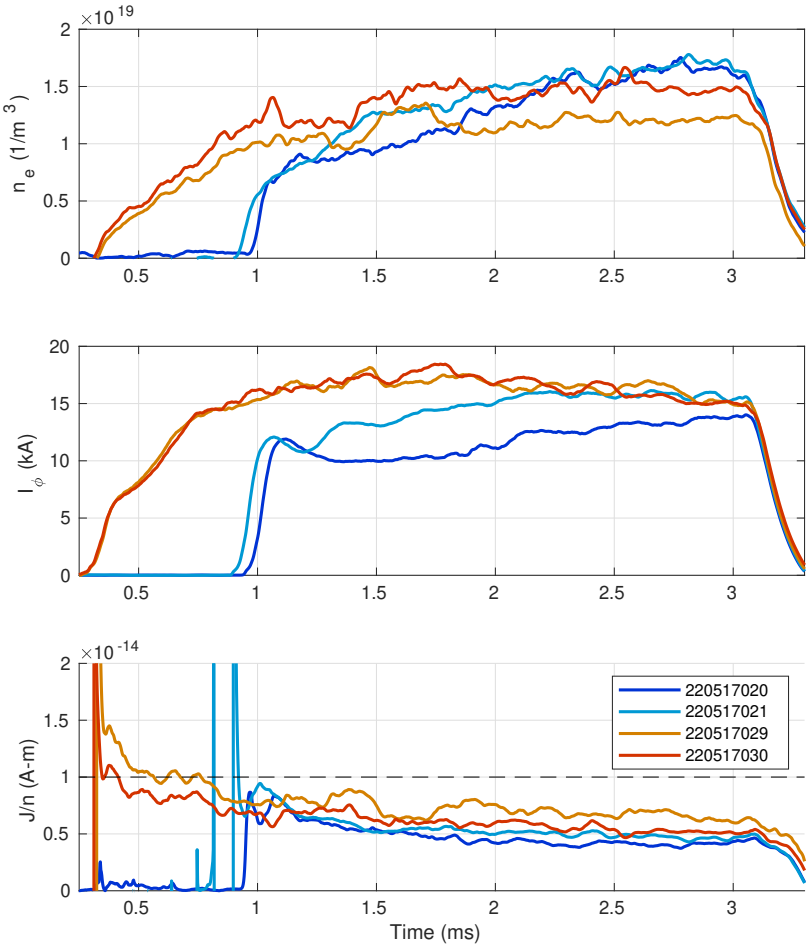

Figure 4.2: Two pairs of HIT-SIU discharges using different fueling types. Shots 22051702 and 220517021 (light and dark blue) employ puff valves only. Shots 220517029 and 220517030 (yellow and orange) use plasma sources and puff valves.

4.2 Plasma-material interactions

During this preliminary low-power study, the high speed cameras on the reentrant ports observed energetic, localized light emission and apparent material sputtering from the inside

walls of the plasma sources. They appear and disappear with the injector cycle, but are not necessarily aligned with the injector electric field or a fixed phase in the cycle. The life cycle of this phenomenon is shown in figure 4.3. It starts as a point on the interior surface, far brighter than the surrounding plasma, and emitting a visible jet of material. When the jet impacts the opposite wall, a similar bright spot forms, connected to the first.

This phenomenon appears most similar to an arc discharge, beginning at a point with surface properties favorable to field emission, then slowly spreading outward as this surface heats up and thermionic emission becomes dominant. The observed "connection" between the two opposite points may be due to the jet from the first point heating the other side [21]. This suggests that a large current is traveling between two conductive surfaces. The spectrometer recorded the presence of ionized copper and iron, but not aluminum, meaning that the most likely candidates are the exposed copper surface of the flux conserver inside the port or the stainless steel interior surface of the flange connecting the glass housing of the plasma source to the manifold. The dielectric alumina coating that prevents plasma currents from jumping to the walls of the flux conserver does not completely cover the inside walls of the port. Large currents are known to flow through the flux conserver and are perturbed to some degree by the hole for the port, given that current must flow around the port. Another possibility initially considered is arcs jumping from the front to the back of the plasma source. During simultaneous operation of the plasma sources and the helicity injectors, a DC offset was observed between the flux conserver and the rear metallic component of the source housing, containing the puff valves. Distinguishing between possible paths was complicated by the fact that it is hard to tell if the bright spots seen in the high-speed camera footage are from the front or the back of the source housing. For this reason, the plasma sources were then removed for visual inspection and to design additional insulation. Surface damage was observed on the inside of both the stainless front section of the source housing and the hole in the flux conserver (see figure 4.4). No such markings were observed on the back section of the housing.

Since these discharges were likely sputtering and vaporizing a significant amount of metal,

operations were discontinued until they could be identified and suppressed. Line radiation is a dominant energy loss mechanism in HIT-SI spheromaks, so performance will be greatly reduced by the presence of high-Z impurities like copper and iron. Additionally, there is also a longer-term danger of sputtered material building up on top of the alumina coating inside the helicity injection manifold. If this dielectric coating were compromised, a significant portion of the plasma current could jump to the wall, drastically reducing performance and further damaging the machine.

To allow HIT-SIU to operate with plasma source fueling in the future, a set of ceramic inserts were designed to prevent these arc events. The design is shown in figure 4.5. They will be made from alumina, and be secured inside the mouth by three alumina set screws. The outside diameter is flared to ensure it sits inside the port at the right position to cover the entire exposed metal surface. It is hoped that blocking line of sight between exposed metal surfaces on opposite sides of the port will prevent arcs by making the resistance of the initial path so high that currents in the flux conserver will bypass the port. At the very least, these inserts will prevent ejecta from one arcing site from setting off another discharge on the opposite side.

4.3 Alternate Modes of HIT-SIU Operation

Due to the lag time involved in getting these inserts custom-made, HIT-SIU operation continued using alumina-coated plugs in place of the plasma sources, shown in figure 4.6. While this removed the possibility of source-assisted breakdown, the design of HIT-SIU, with the helicity injectors combined into a single manifold, allows a new operating mode where the injectors operate in-phase with each other, acting as a single toroidal confinement structure, similar to a reversed-field pinch (RFP) where the flux coils act as toroidal field coils and the voltage coils act like the transformer coils. The high-speed feedback control system is then able to transition to a more standard mode, where the helicity injectors operate out of phase with each other, either in two pairs separated by 180 degrees of phase, or individually, separated by 90 degrees, both of which inject energy and helicity into the flux conserver [27].

Starting in this RFP mode can aid in achieving breakdown, since it provides a much longer path, with less ripple, for electrons to accelerate. In this mode, HIT-SIU has been able to operate at puff valve pressures as low as 1500 Torr. This is not as low as the plasma sources were able to achieve breakdown at, even with high magnetic field, but still much lower than HIT-SI3 was able to reliably operate at. Two methods were tried to improve further on this operating regime. First, the original plasma source retained from HIT-SI3 was employed, but there was no noticeable improvement due to its location far from the injectors. Next, the initial phase difference between the flux and voltage coils was varied, based on the idea of ramping up the electric field slightly before the magnetic field will result in longer electron path lengths. This did not allow any significant drop in operating pressure but a phase difference of 10 degrees did allow a small but significant improvement in breakdown time and reliability.

When operating in the injector-RFP mode, HIT-SIU also behaved very differently from HIT-SI3 when varying the duration of the gas puff valves. HIT-SI3 typically had to operate with puff valves open for most of the discharge duration, to avoid starving the injectors. This "starvation" occurs when the current flowing through the helicity injectors becomes limited by the available plasma density, rather than supplied power. However, HIT-SIU is able to operate with a much shorter duration of fueling, or even shutting off the puff valves before the discharge begins, without showing any evidence of injector starvation. Figure 4.7 shows an example of a low density HIT-SI discharge which displayed this "starvation" effect, compared to a recent HIT-SIU high power discharge. HIT-SIU is able to operate with much more consistant density, without any signs that toriodal current is being restricted. The pre-ionization sources are one of several features that HIT-SIU was designed with to control density and avoid starvation. It is likely that even without them installed, excess plasma and neutrals are able to flow between them, rather than being vented into the confinement volume on each cycle. The phase separation of the injectors means that the point in the cycle where one is most strongly expelling plasma (due to flux reversal) is also the point its neighbor's can accept density at peak flux.

Thus far, operation in this parameter space has demonstrated improved density control and consistency when compared with previous experiments. HIT-SIU has been able to operate with density near or slightly below the Greenwald limit for most of the discharge, but not much further than that. It is possible that this will only be achieved by running at even lower pressure, once the pre-ionization sources are reinstalled with the inserts to prevent surface arcs. However, recent results suggest that reinstalling the pre-ionization sources may improve performance in another way. Figure 4.8 shows that at breakdown, when injector current jumps up, the voltage in the coils driving current drops precipitously, indicating that the vast majority of the power in the circuit is being taken up by ionizing the gas present inside. It takes nearly half a millisecond for the voltage to climb back up to nominal levels. If most of the energy for ionization was being provided by the pre-ionization sources, it could greatly improve power utilization in the early stages of the discharge and during the phase transition from injector-RFP to spheromak operation.

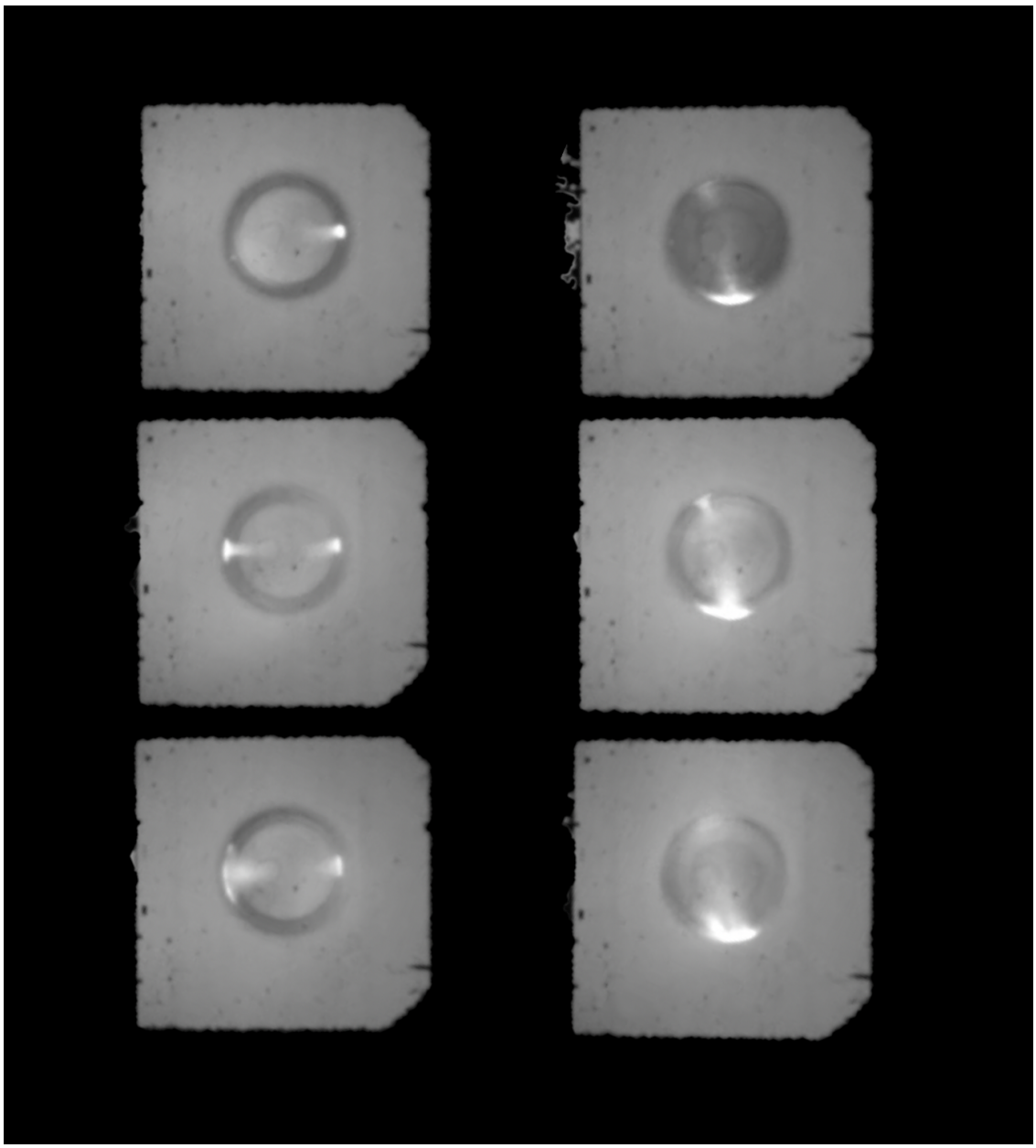

Figure 4.3: Two examples (left and right) of transient plasma-material interactions inside the HIT-SIU plasma sources captured using a Phantom v1212 high-speed camera. Top images capture the beginning of the observed discharges, center are midway through, and bottom images are when the discharges are starting to fade away.

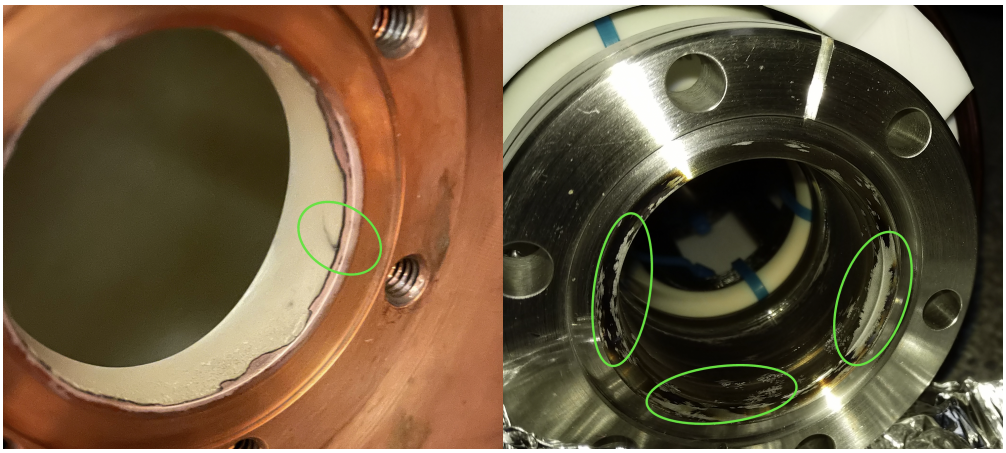

Figure 4.4: Surface damage observed on the inside surfaces of the flux conserver port and the front section of the source housing.

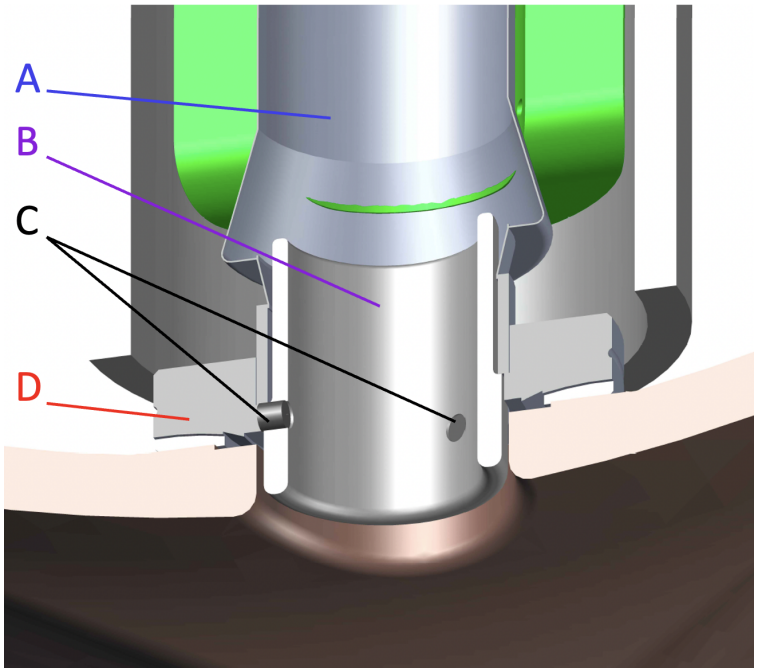

Figure 4.5: Design of ceramic inserts for pre-ionization sources. A: Glass housing, B: Ceramic insert, C: Ceramic set screws securing ceramic insert, D: front (stainless) section of source housing.

Figure 4.6: Two of the plugs used in place of pre-ionization sources, before and after the alumina coating was applied.

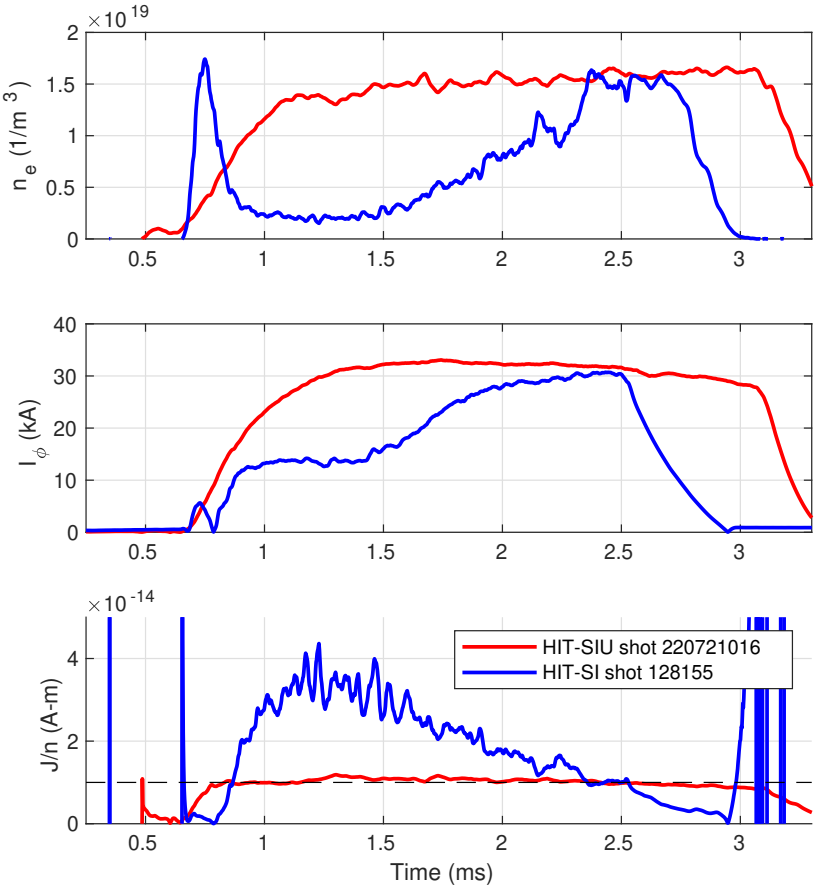

Figure 4.7: Comparison between a low density HIT-SI discharge and a more recent HIT-SIU discharge. Note that for the blue curve, current is depressed in the region where density is low.

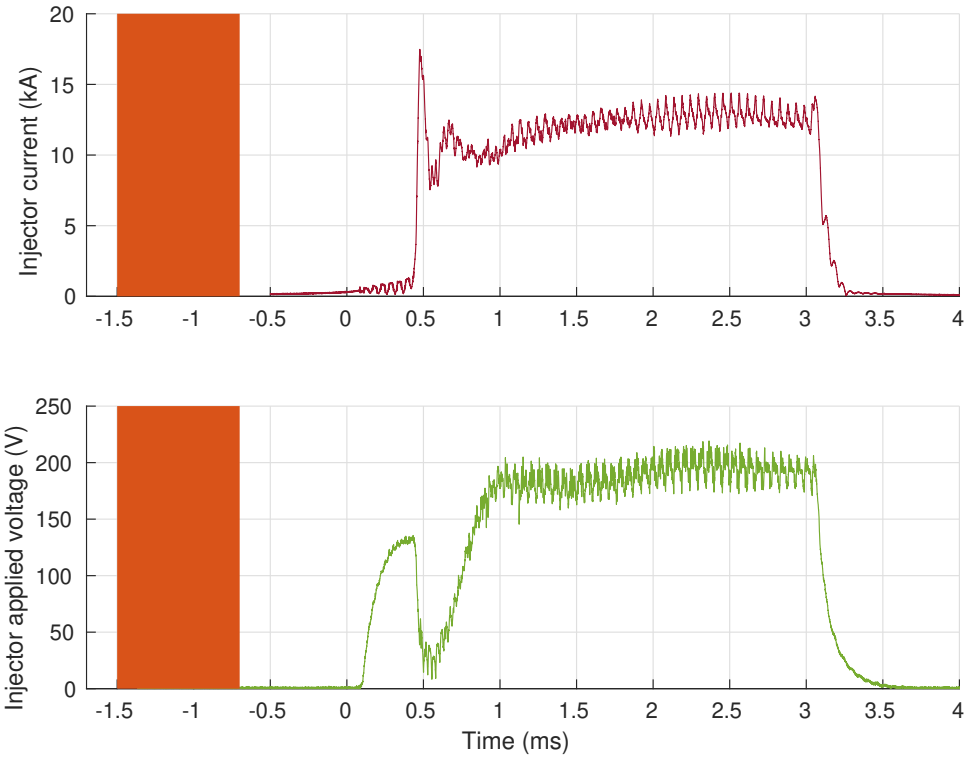

Figure 4.8: Injector plasma current and applied voltage during a HIT-SIU discharge in injector-RFP to spheromak mode. The orange regions indicate the points where the puff valves are switched on and off. Note that puff valve fueling stops significantly before the discharge even begins, and voltage drops steeply during breakdown.

Chapter 5

CONCLUSION AND FUTURE WORK

SIHI-driven spheromaks have several attractive properties for development into a future nuclear fusion power reactor. The combination of high beta, efficient current drive, and steady-state operation could enable more compact and cost-effective reactors than many of the more conventional confinement configurations. The final campaign of HIT-SI3 and the initial campaign of HIT-SIU have made great strides in improving their capability as a demonstration platform for SIHI-driven spheromaks. In addition to reaching record values of current gain, HIT-SI3 has demonstrated that there is a lot of room for improvement when it comes to fueling the helicity injectors while preventing excess neutral gas building up in the confinement volume. Comparing Langmuir probe data to a 1D multi-fluid transport model is not fully conclusive, but suggests that neutral density in the edge plasma region is higher than previous modeling studies indicated. HIT-SIU was designed with several improvements to address this problem. The high power inductively coupled plasma sources designed as a new fueling source are able to consistently supply a dense, warm ($\approx$ 10 eV) plasma to the helicity injectors, and is able to achieve breakdown at a much lower density than either HIT-SI3 or HIT-SIU have ever been able to achieve using puff valves alone. Its performance has been characterized across a range of magnetic field strengths and pressures in both working gasses, allowing parameters to be tuned to what is most suitable to future full-power studies, done after diagnostics have been removed.

During initial spheromak operations using the plasma sources for fueling, HIT-SIU displayed faster and more reliable breakdown, as well as superior control of density. However, plasma-material interactions were also identified that posed a risk for future operations. A mitigation strategy was developed using high-speed camera results and inspections of com-

ponent surfaces to identify the sites of these interactions. The components needed to implement this fix were designed and are being manufactured. More recent high-power studies have shown that HIT-SIU is much more amenable to operation at low power than expected, but the pre-ionization sources are still expected to be beneficial, by allowing operation at even lower pressures, and providing energy for ionization, reducing the load on the injector circuits.

Beyond operating at higher power and lower density, HIT-SIU can repeat the neutral transport studies done on HIT-SI3 to get a better understanding of the differences between them. If a fast ionization pressure gauge is available, it will show what difference, if any, there is between HIT-SI3 and HIT-SIU in how neutral gas is forced out of the injectors. Another Langmuir probe study in the passive pumping volume could also demonstrate a difference in neutral density of the edge plasma region. The 1D plasma-neutral transport model shows that lower neutral density results in slower falloff of plasma density, due to weaker plasma-neutral coupling. If Langmuir probe data showed this slower falloff, it would indicate substantially lower neutral density in the edge region.

BIBLIOGRAPHY

[1] K. Burm. Breakdown magnetic field in an inductively coupled plasma. *Physics Letters A*, 2008.

[2] J. C. Santamarina C. Pasten. Energy and quality of life. *Energy Policy*, 2012.

[3] J. F. Caneses and B. Blackwell. Rf compensation of langmuir probes: modelling and experiment. *Plasma Sources science and technology*, 24, 2015.

[4] F. F. Chen and D. Arnush. Generalized theory of helicon waves i. normal modes. *Physics of plasmas*, 1997.

[5] F. F. Chen and D. Arnush. Generalized theory of helicon waves ii. excitation and absorbtion. *Physics of plasmas*, 1998.

[6] K. S. Chung. A kinetic theory of ion collection by probe in flowing unmagnetized plasma. *Journal of applied physics*, 1991.

[7] K. S. Chung. Mach probes. *Plasma sources science and technology*, 1991.

[8] D. Elliot, D. Sutherland, U. Siddiqui, E. Scime, C. Everson, K. Morgan, A. Hossack, B. Nelson, and T. Jarboe. Two-photon lif on the hit-si3 experiment: Absolute density and temperature measurements of deuterium neutrals. *Review of Scientific Instruments*, 87:11E506, 2016.

[9] J Green. *Neutral Dynamics in a Helicon Plasma*. PhD thesis, University of Wisconsin, 2019.

[10] M. Greenwald. Density limits in toroidal plasmas. *Plasma Physics and Controled Fusion*, 22, July 2002.

[11] C. Hansen, G. Marklin, B. Victor, C. Akcay, and T. Jarboe. Simulation of injector dynamics during steady inductive helicity injection current drive in the hit-si experiment. *Physics of Plasmas*, 22(4):042505, 2015.

[12] C. J. Hansen. *MHD Modeling in Complex 3D Geometries: Towards Predictive Simulation of SIHI Current Drive*. PhD thesis, University of Washington, 2014.

[13] J. S. Hardwick. *Ohmic Ignition in a spheromak*. Phd Thesis. University of California at Berkeley, 1996.

[14] A. C. Hossack. *A Study of Plasma Dynamics in HIT-SI using Ion Doppler Spectroscopy*. PhD thesis, University of Washington, 2015.

[15] A. C. Hossack, T. Firman, T. R. Jarboe, J. R. Prager, B. S. Victor, J. S. Wrobel, and T. Ziemba. Reduction of plasma density in the helicity injected torus with steady inductance experiment by using a helicon pre-ionization source. *Review of Scientific Instruments*, 84(10):103506, 2013.

[16] A. C. Hossack, K. D. Morgan, C. J. Hansen, and D. A. Sutherland. A multi-chord, two-color interferometer using hilbert transform phase detection for measuring electron density in spheromak plasmas. *To Appear: Review of Scientific Instruments*, 2022.

[17] I. H. Hutchinson. *Principles of plasma diagnostics*. Cambridge University press, 2002.

[18] T.R. Jarboe, B.S. Victor, B.A. Nelson, C.J. Hansen, C. Akcay, D.A. Ennis, N.K. Hicks, A.C. Hossack, G.J. Marklin, and R.J. Smith. Imposed-dynamo current drive. *Nuclear Fusion*, 52(8):083017, jul 2012.

[19] N. S. Kardashev. *On the Inevitability and Possible Structures of Supercivilizations*. International Astronomical Union, 1985.

[20] I. A. Kotelnikov. On the density limit in helicon plasma sources. *Physics of plasmas*, 2014.

[21] M. A. Lieberman and A. J. Lichtenberg. *Principles of Plasma Discharges and Materials Processing*. John Wiley and Sons, 2005.

[22] M. Q. Tran M. Kikuchi, K. Lackner. *Fusion Physics*. IAEA, 2012.

[23] H. S. McLean, S. Woodruff, E. B. Hooper, R. H. Bulmer, D. N. Hill, C. Holcomb, J. Moller, B. W. Stallard, R. D. Wood, and Z. Wang. Suppression of mhd fluctuations leading to improved confinement in a gun-driven spheromak. *Phys. Rev. Lett.*, 88:125004, Mar 2002.

[24] E. T. Meier and U. Shumlak. A general nonlinear model for mixing plasma-neutral mittures. *Plasma Physics*, 2012.

[25] D. G. Miljak and F. F. Chen. *Helicon wave excitation with rotating antenna fields*. University of California, Los Angeles, 1997.

[26] K. D. Morgan. *Finite-beta Simulations of HIT-SI and HIT-SI3 using the NIMROD Code*. PhD thesis, University of Washington, 2015.

[27] K. D. Morgan, A. C. Hossack, C. J. Hansen, B. A. Nelson, and D. A. Sutherland. High-speed feedback control of an oscillating magnetic helicity injector using a graphics processing unit. *Review of Scientific Instruments*, 92(5):053530, 2021.

[28] M. Y. Naz et al. Double and triple langmuir probe measurements in inductively coupled nitrogen plasma. *Progress in electromagnetics research*, 2011.

[29] United Nations Department of Social and Population Divisions Economic Affairs. World population prospects 2019. Technical report, United Nations, 2019.

[30] R. G. O'Neil. *An Experimental Study of Helicity Injection Current Drive in the HIT-SI Spheromak*. PhD Thesis, University of Washington, 2007.

[31] ITER Organization. Neutral beams: the system that makes the tokamak feel small. `https://www.iter.org/newsline/-/3254`, 2019.

[32] H. O. Pörtner et al. Climate change 2022: Impacts, adaptation, and vulnerability. contribution of working group ii to the sixth assessment report of the intergovernmental panel on climate change. 2022.

[33] Nestor A. Sepulveda, Jesse D. Jenkins, Fernando J. de Sisternes, and Richard K. Lester. The role of firm low-carbon electricity resources in deep decarbonization of power generation. *Joule*, 2(11):2403–2420, 2018.

[34] S. Shinohara and H. Mizokoshi. Development of a strong field helicon plasma source. *Review of scientific instruments*, 2005.

[35] P. E Sieck. *Spheromak Formation Using Steady-Inductive Helicity Injection*. PhD Thesis, University of Washington, 2006.

[36] T. H. Stix. *Waves in plasmas: Highlights from the past and present*. Princeton plasma physics laboratory, 1992.

[37] D. A. Sutherland. *Measurements of neutral particles and simulations of plasma-neutral interactions in the HIT-SI3 experiment*. PhD thesis, University of Washington, 2019.

[38] D.A. Sutherland, T.R. Jarboe, K.D. Morgan, M. Pfaff, E.S. Lavine, Y. Kamikawa, M. Hughes, P. Andrist, G. Marklin, and B.A. Nelson. The dynomak: An advanced spheromak reactor concept with imposed-dynamo current drive and next-generation nuclear power technologies. *Fusion Engineering and Design*, 89(4):412–425, 2014.

[39] J. B. Taylor. Relaxation of toroidal plasma and generation of reverse magnetic fields. *Physical Review Letters*, 33:1139–1141, Nov 1974.

[40] Shengwu Zhang, Yiwen Li, Wang Ma, Xiaolong Wei, and Wenyuan Zhang. Effects of axial magnetic field on discharge characteristics of inductively coupled plasma. *AIP Advances*, 10(5):055209, 2020.

Appendix A

EQUATIONS FOR PLASMA-NEUTRAL TRANSPORT MODEL

A.1 Definitions

The definitions for the following properties are given in the same way as in [38]

Ionization and recombination rates

$$< \sigma_{iz} v_e >= \frac{2 \cdot 10^{-13}}{6 + \frac{T_e}{13.6}} \frac{T_e}{13.6} e^{\frac{-13.6}{T_e}} \tag{A.1}$$

$$< \sigma_{rc} v_e >= 7 \cdot 10^{-20} \sqrt{\frac{13.6}{T_e}} \tag{A.2}$$

Charge-exchange cross section

$$\sigma_{cx} = (1.09 \cdot 10^{-18} - 7.15 \cdot 10^{-20} \ln V_{cx}) \tag{A.3}$$

$$V_{cx} = \sqrt{\frac{28}{5 m_i}(k T_i + k T_n) + (V_i - V_n)^2} \tag{A.4}$$

Momentum transfer due to charge-exchange

$$r_{in} = \sigma_{cx} \frac{\gamma k T_n}{m_i} \frac{1}{\sqrt{\frac{56 k T_i}{5 \pi m_i} + \frac{63 \pi k T_n}{20 m_i} + 4(V_i - V_n)^2}} \tag{A.5}$$

$$r_{ni} = \sigma_{cx} \frac{7 k T_i}{5 m_i} \frac{1}{\sqrt{\frac{56 k T_n}{5 \pi m_i} + \frac{63 \pi k T_i}{20 m_i} + 4(V_i - V_n)^2}} \tag{A.6}$$

Heat gain/loss due to ionization and recombination

$$q_{iz} =< \sigma_{iz} v_e > \frac{3}{2} k T_n \tag{A.7}$$

$$q_{rc} =< \sigma_{rc} v_e > \frac{3}{2} k T_i \tag{A.8}$$

heat transfer due to charge-exchange

$$q_{in} = \frac{21kT_n}{20m_i}\sqrt{\frac{28kT_i}{5\pi m_i} + \frac{448kT_n}{45\pi m_i} + (V_i - V_n)^2} \tag{A.9}$$

$$q_{ni} = \frac{21kT_i}{20m_i}\sqrt{\frac{28kT_n}{5\pi m_i} + \frac{448kT_i}{45\pi m_i} + (V_i - V_n)^2} \tag{A.10}$$

In addition, a wall loss term is introduced as a cross-section, depending on the diameter of the pumping volume d

$$\sigma_{wall} = \frac{1}{d\sqrt{\pi}} \tag{A.11}$$

So that the plasma flux to the wall is

$$\Gamma_{pi} = \sigma_{wall} V_{Bohm} \tag{A.12}$$

And the neutral flux to the wall is

$$\Gamma_n = \sigma_{wall} v_{n_{th}} \tag{A.13}$$

A.2 Zeroth moment

The density evolution for both fluids is given by the continuity equations, including the wall term

$$\frac{\partial n_i}{\partial t} = D\frac{\partial^2 n_i}{\partial x^2} - V_i\frac{\partial n_i}{\partial x} + n_i n_n < \sigma_{iz} v_e > - n_i^2 < \sigma_{rc} v_e > - n_i \sigma_{wall} v_{Bohm} \tag{A.14}$$

$$\frac{\partial n_n}{\partial t} = D\frac{\partial^2 n_n}{\partial x^2} - V_n\frac{\partial n_n}{\partial x} - n_i n_n < \sigma_{iz} v_e > + n_i^2 < \sigma_{rc} v_e > + n_i \sigma_{wall} v_{Bohm} \tag{A.15}$$

A.3 First moment

Velocity evolution is given by multiplying the continuity equations by mV, and adding in pressure and charge-exchange terms

$$\begin{aligned}\frac{\partial}{\partial t}(m_i n_i V_i) + \frac{\partial}{\partial x}(m_i n_i V_i V_i + P) = \\ + n_i n_n < \sigma_{iz} v_e > m_i V_n - n_i^2 < \sigma_{rc} v_e > m_i V_i \\ + n_i n_n \sigma_{cx} V_{cx} m_i (V_n - V_i) + m_i n_i n_n (V_n - V_i)(r_{in} + r_{ni}) \\ - n_i \sigma_{wall} v_{Bohm} m_i V_i\end{aligned} \tag{A.16}$$

$$\begin{aligned}\frac{\partial}{\partial t}(m_i n_n V_n) + \frac{\partial}{\partial x}(m_i n_n V_n V_n + P) = \\ - n_i n_n < \sigma_{iz} v_e > m_i V_n + n_i^2 < \sigma_{rc} v_e > m_i V_i \\ + n_i n_n \sigma_{cx} V_{cx} m_i (V_i - V_n) + m_i n_i n_n (V_i - V_n)(r_{ni} + r_{in}) \\ - n_n \sigma_{wall} v_{n_{th}} m_i V_n\end{aligned} \tag{A.17}$$

Applying the chain rule

$$\begin{aligned}m_i n_i \frac{\partial V_i}{\partial t} + m_i V_i \frac{\partial n_i}{\partial t} + m_i V_i \frac{\partial V_i}{\partial x} + m_i V_i \frac{\partial}{\partial x}(n_i V_i) = \\ - 2\frac{\partial}{\partial x}(n_i k T_i) + n_i n_n < \sigma_{iz} v_e > m_i V_n - n_i^2 < \sigma_{rc} v_e > m_i V_i \\ + n_i n_n \sigma_{cx} V_{cx} m_i (V_n - V_i) + m_i n_i n_n (V_n - V_i)(r_{in} + r_{ni}) \\ - n_i \sigma_{wall} v_{Bohm} m_i V_i\end{aligned} \tag{A.18}$$

$$\begin{aligned}m_i n_n \frac{\partial V_n}{\partial t} + m_i V_n \frac{\partial n_n}{\partial t} + m_i V_n \frac{\partial V_n}{\partial x} + m_i V_n \frac{\partial}{\partial x}(n_n V_n) = \\ - \frac{\partial}{\partial x}(n_n k T_n) - n_i n_n < \sigma_{iz} v_e > m_i V_n + n_i^2 < \sigma_{rc} v_e > m_i V_i \\ + n_i n_n \sigma_{cx} V_{cx} m_i (V_i - V_n) + m_i n_i n_n (V_i - V_n)(r_{ni} + r_{in}) \\ - n_n \sigma_{wall} v_{n_{th}} m_i V_n\end{aligned} \tag{A.19}$$

Substituting in continuity equation to eliminate the terms containing $\frac{\partial n_i}{\partial t}$. This introduces a

second wall term

$$\begin{aligned} m_i n_i(\frac{\partial V_i}{\partial t} + V_i\frac{\partial V_i}{\partial x}) = \\ &- 2\frac{\partial}{\partial x}(n_i k T_i) - m_i V_i(n_i n_n < \sigma_{iz} v_e > - n_i^2 < \sigma_{rc} v_e > \\ &- n_i \sigma_{wall} v_{Bohm}) + n_i n_n < \sigma_{iz} v_e > m_i V_n - n_i^2 < \sigma_{rc} v_e > m_i V_i \\ &+ n_i n_n \sigma_{cx} V_{cx} m_i (V_n - V_i) + m_i n_i n_n (V_n - V_i)(r_{in} + r_{ni}) \\ &- n_i \sigma_{wall} v_{Bohm} m_i V_i \end{aligned} \tag{A.20}$$

$$\begin{aligned} m_i n_n(\frac{\partial V_n}{\partial t} + V_n\frac{\partial V_n}{\partial x}) = \\ &- \frac{\partial}{\partial x}(n_n k T_n) - m_i V_n(-n_i n_n < \sigma_{iz} v_e > + n_i^2 < \sigma_{rc} v_e > \\ &+ n_i \sigma_{wall} v_{Bohm}) - n_i n_n < \sigma_{iz} v_e > m_i V_n + n_i^2 < \sigma_{rc} v_e > m_i V_i \\ &+ n_i n_n \sigma_{cx} V_{cx} m_i (V_i - V_n) + m_i n_i n_n (V_i - V_n)(r_{ni} + r_{in}) \\ &- n_n \sigma_{wall} v_{n_{th}} m_i V_n \end{aligned} \tag{A.21}$$

Simplify and define neutral thermal velocity $v_{n_{th}}$ as $\sqrt{\frac{7kT_n}{5m_i}}$ for diatomic gas

$$\begin{aligned} \frac{\partial V_i}{\partial t} = D\frac{\partial^2 V_i}{\partial x^2} - V_i\frac{\partial V_i}{\partial x} - \frac{2}{m_i n_i}\frac{\partial}{\partial x}(n_i k T_i) \\ + n_n(V_n - V_i)(< \sigma_{iz} v_e > + \sigma_{cx} V_{cx} + r_{in} + r_{ni}) \end{aligned} \tag{A.22}$$

$$\begin{aligned} \frac{\partial V_n}{\partial t} = D\frac{\partial^2 V_n}{\partial x^2} - V_n\frac{\partial V_n}{\partial x} - \frac{1}{m_i n_n}\frac{\partial}{\partial x}(n_n k T_n) \\ + n_i(V_i - V_n)(\frac{n_i}{n_n} < \sigma_{rc} v_e > + \sigma_{cx} V_{cx} + r_{ni} + r_{in}) \\ - V_n \sigma_{wall}(\frac{n_i}{n_n} v_{Bohm} + \sqrt{\frac{7kT_n}{5m_i}}) \end{aligned} \tag{A.23}$$

A.4 Second Moment

Temperature evolution is given by multiplying the continuity equations by $\frac{1}{2}m_s n_s V_s^2$, adding in pressure and wall terms

$$\begin{aligned}\frac{\partial}{\partial t}(\frac{P_i}{\gamma-1})+\frac{\partial}{\partial x}(\frac{P_i}{\gamma-1}V_i)+\frac{\partial}{\partial t}(\frac{1}{2}m_i n_i V_i^2)+\frac{\partial}{\partial x}(\frac{1}{2}m_i n_i V_i^2 V_i)=\\ -\frac{\partial}{\partial x}(V_i P_i)+n_i n_n<\sigma_{iz}v_e>(\frac{1}{2}m_i V_n^2-\phi_{iz})-n_i^2<\sigma_{rc}v_e>(\frac{1}{2}m_i V_i^2)\\ +n_i n_n\frac{1}{2}\sigma_{cx}V_{cx}m_i(V_n^2-V_i^2)+V_n m_i n_i n_n(V_n-V_i)r_{in}+V_i m_i n_i n_n(V_n-V_i)r_{ni}\\ +n_i n_n q_{iz}-n_i^2 q_{rc}+n_i n_n\frac{3}{4}(q_{in}-q_{ni})-n_i\sigma_{wall}V_{Bohm}\frac{1}{2}m_i V_i^2\end{aligned} \tag{A.24}$$

$$\begin{aligned}\frac{\partial}{\partial t}(\frac{P_n}{\gamma-1})+\frac{\partial}{\partial x}(\frac{P_n}{\gamma-1}V_n)+\frac{\partial}{\partial t}(\frac{1}{2}m_i n_n V_n^2)+\frac{\partial}{\partial x}(\frac{1}{2}m_i n_n V_n^2 V_n)=\\ -\frac{\partial}{\partial x}V_n P_n-n_i n_n<\sigma_{iz}v_e>\frac{1}{2}m_i V_n^2+n_i^2<\sigma_{rc}v_e>(\frac{1}{2}m_i V_n^2)\\ +n_i n_n\sigma_{cx}V_{cx}m_i(V_i^2-V_n^2)+V_n m_i n_i n_n(V_i-V_n)r_{in}+V_i m_i n_i n_n(V_i-V_n)r_{ni}\\ -n_i n_n q_{iz}+n_i^2 q_{rc}+n_i n_n\frac{3}{4}(q_{ni}-q_{in})-n_n\sigma_{wall}\sqrt{\frac{\gamma k T_n}{m_i}}\frac{1}{2}m_i V_n^2.\end{aligned} \tag{A.25}$$

Apply the chain rule to pressure terms on the left hand side

$$\begin{aligned}\frac{\partial}{\partial t}(\frac{P_i}{\gamma-1})+\frac{\partial}{\partial x}(\frac{P_i}{\gamma-1}V_i)=\\ \frac{2}{\gamma-1}(n_i\frac{\partial T_i}{\partial t}+T_i\frac{\partial n_i}{\partial t})+n_i V_i\frac{\partial}{\partial x}(\frac{2T_i}{\gamma-1})+\frac{2T_i}{\gamma-1}\frac{\partial}{\partial x}(n_i V_i)\end{aligned} \tag{A.26}$$

$$\begin{aligned}\frac{\partial}{\partial t}(\frac{P_i}{\gamma-1})+\frac{\partial}{\partial x}(\frac{P_i}{\gamma-1}V_n)=\\ \frac{1}{\gamma-1}(n_n\frac{\partial kT_n}{\partial t}+kT_n\frac{\partial n_n}{\partial t})+n_n V_n\frac{\partial}{\partial x}(\frac{kT_n}{\gamma-1})+\frac{kT_n}{\gamma-1}\frac{\partial}{\partial x}(n_n V_n)\end{aligned} \tag{A.27}$$

Simplify and substitute continuity equation

$$\frac{2n_i}{\gamma-1}\frac{\partial kT_i}{\partial t}+\frac{2n_i}{\gamma-1}V_i\frac{\partial kT_i}{\partial x}+\frac{2kT_i}{\gamma-1}(\frac{\partial n_i}{\partial t}+\frac{\partial}{\partial x}(n_iV_i))= \\ \frac{2n_i}{\gamma-1}(\frac{\partial kT_i}{\partial t}+V_i\frac{\partial kT_i}{\partial x})+\frac{2kT_i}{\gamma-1}(n_in_n<\sigma_{iz}v_e>-n_i^2<\sigma_{rc}v_e>-n_i\sigma_{wall}V_{Bohm}) \tag{A.28}$$

$$\frac{n_n}{\gamma-1}\frac{\partial kT_n}{\partial t}+\frac{n_n}{\gamma-1}V_n\frac{\partial kT_n}{\partial x}+\frac{kT_n}{\gamma-1}(\frac{\partial n_n}{\partial t}+\frac{\partial}{\partial x}(n_nV_n))= \\ \frac{n_n}{\gamma-1}(\frac{\partial kT_n}{\partial t}+V_n\frac{\partial kT_n}{\partial x})+\frac{kT_n}{\gamma-1}(-n_in_n<\sigma_{iz}v_e>+n_i^2<\sigma_{rc}v_e>+n_i\sigma_{wall}V_{Bohm}) \tag{A.29}$$

To substitute for kinetic energy terms, multiply momentum equation by V

$$V_i\frac{\partial}{\partial t}(m_in_iV_i)+V_n\frac{\partial}{\partial x}(m_in_iV_iV_i)= \\ -V_i\frac{\partial}{\partial x}P_i+V_i<\sigma_{iz}v_e>m_iV_n-V_i<\sigma_{re}v_e>m_iV_i \\ +V_i\sigma_{cx}V_{cx}m_i(V_n-V_i)+V_im_in_in_n(V_n-V_i)(r_{in}+r_{ni})-V_in_i\sigma_wV_{Bohm}m_iV_i \tag{A.30}$$

$$V_n\frac{\partial}{\partial t}(m_in_nV_n)+V_n\frac{\partial}{\partial x}(m_in_nV_nV_n)= \\ -V_n\frac{\partial}{\partial x}P_n-V_n<\sigma_{iz}v_e>m_iV_n+V_n<\sigma_{re}v_e>m_iV_i \\ +V_n\sigma_{cx}V_{cx}m_i(V_i-V_n)+V_nm_in_in_n(V_i-V_n)(r_{ni}+r_{in})-V_nn_n\sigma_w\frac{\gamma kT_n}{m_i}m_iV_n \tag{A.31}$$

Apply chain rule to kinetic energy equation

$$\frac{\partial}{\partial t}(\frac{1}{2}m_in_iV_i^2)+\frac{1}{2}m_iV_i^2\frac{\partial n_i}{\partial t}+\frac{\partial}{\partial x}(\frac{1}{2}m_in_iV_iV_i^2)+\frac{1}{2}m_iV_i^2\frac{\partial}{\partial x}(n_iV_i)= \\ -V_i\frac{\partial}{\partial x}P_i+V_i<\sigma_{iz}v_e>m_iV_n-V_i<\sigma_{re}v_e>m_iV_i \\ +V_i\sigma_{cx}V_{cx}m_i(V_n-V_i)+V_im_in_in_n(V_n-V_i)(r_{in}+r_{ni})-V_in_i\sigma_{wall}V_{Bohm}m_iV_i \tag{A.32}$$

$$\frac{\partial}{\partial t}(\frac{1}{2}m_i n_n V_n^2) + \frac{1}{2}m_i V_n^2 \frac{\partial n_n}{\partial t} + \frac{\partial}{\partial x}(\frac{1}{2}m_i n_n V_n V_n^2) + \frac{1}{2}m_i V_n^2 \frac{\partial}{\partial x}(n_n V_n) =$$
$$- V_n \frac{\partial}{\partial x} P_n - V_n < \sigma_{iz} v_e > m_i V_n + V_n < \sigma_{re} v_e > m_i V_i$$
$$+ V_n \sigma_{cx} V_{cx} m_i (V_i - V_n) + V_n m_i n_i n_n (V_i - V_n)(r_{ni} + r_{in}) - V_n n_n \sigma_{wall} \frac{\gamma k T_n}{m_i} m_i V_n \tag{A.33}$$

Substitute continuity equation to eliminate ∂n terms

$$\frac{\partial}{\partial t}(\frac{1}{2}m_i n_i V_i^2) + \frac{\partial}{\partial x}(\frac{1}{2}m_i n_i V_i V_i^2) =$$
$$\frac{1}{2}m_i V_i^2 n_i n_n < \sigma_{iz} v_e > - \frac{1}{2}m_i V_i^2 n_i^2 < \sigma_{rc} v_e > - \frac{1}{2}m_i V_i^2 n_i \sigma_w V_{Bohm}$$
$$- V_i \frac{\partial}{\partial x} P_i + n_i n_n < \sigma_{iz} v_e > m_i V_n V_i - n_i^2 < \sigma_{rc} v_e > m_i V_i^2 \tag{A.34}$$
$$+ m_i n_i n_n (\sigma_{cx} V_{cx} + r_{in} + r_{ni})(V_i V_n - V_i^2) - m_i V_i^2 n_i \sigma_w V_{Bohm}$$

$$\frac{\partial}{\partial t}(\frac{1}{2}m_i n_n V_n^2) + \frac{\partial}{\partial x}(\frac{1}{2}m_i n_n V_n V_n^2) =$$
$$- \frac{1}{2}m_i V_n^2 n_n n_n < \sigma_{iz} v_e > + \frac{1}{2}m_i V_n^2 n_n^2 < \sigma_{rc} v_e > + \frac{1}{2}m_i V_n^2 n_i \sigma_w V_{Bohm}$$
$$- V_n \frac{\partial}{\partial x} P_n - n_i n_n < \sigma_{iz} v_e > m_i V_n^2 + n_i^2 < \sigma_{rc} v_e > m_i V_i V_n \tag{A.35}$$
$$+ m_i n_i n_n (\sigma_{cx} V_{cx} + r_{in} + r_{ni})(V_i V_n - V_n^2) - m_i V_n^2 n_n \sigma_w \frac{\gamma k T_n}{m_i}$$

Simplify kinetic energy equations

$$\frac{\partial}{\partial t}(\frac{1}{2}m_i n_i V_i^2) + \frac{\partial}{\partial x}(\frac{1}{2}m_i n_i V_i V_i^2) =$$
$$- V_i \frac{\partial}{\partial x} P_i + m_i n_i n_n < \sigma_{iz} v_e > (V_n V_i - \frac{1}{2}V_i^2) - n_i^2 < \sigma_{rc} v_e > \frac{1}{2}m_i V_i^2 \tag{A.36}$$
$$+ m_i n_i n_n (\sigma_{cx} V_{cx} + r_{in} + r_{ni})(V_i V_n - V_i^2) + \frac{1}{2}m_i V_i^2 n_i \sigma_w V_{Bohm}$$

$$\frac{\partial}{\partial t}(\frac{1}{2}m_i n_n V_n^2) + \frac{\partial}{\partial x}(\frac{1}{2}m_i n_n V_n V_n^2) =$$
$$- V_n \frac{\partial}{\partial x} P_n - n_i n_n < \sigma_{iz} v_e > m_i V_n^2 + n_i^2 < \sigma_{rc} v_e > m_i (V_i V_n - \frac{1}{2} V_n^2)$$
$$+ m_i n_i n_n (\sigma_{cx} V_{cx} + r_{in} + r_{ni})(V_i V_n - V_n^2) - m_i V_n^2 \sigma_w (\frac{1}{2} n_i V_{Bohm} + n_n \frac{\gamma k T_n}{m_i}) \tag{A.37}$$

Substitute kinetic energy terms and second pressure terms back into initial equation

$$\frac{2n_i}{\gamma - 1}(\frac{\partial k T_i}{\partial t} + V_i \frac{\partial k T_i}{\partial x}) =$$
$$\frac{\partial}{\partial x}(2 V_i n_i k T_i) + n_i n_n < \sigma_{iz} v_e > (\frac{1}{2} m_i V_n^2 - \phi_{iz}) - n_i^2 < \sigma_{rc} v_e > (\frac{1}{2} m_i V_i^2)$$
$$+ \sigma_{cx} V_{cx} \frac{1}{2} m_i (V_n^2 - V_i^2) + V_n m_i n_i n_n (V_i - V_n) r_{in} + V_i m_i n_i n_n (V_i - V_n) r_{ni}$$
$$+ n_i n_n q_{iz} - n_i^2 q_{rc} + n_i n_n \frac{3}{4}(q_{in} - q_{ni}) - n_i \sigma_{wall} V_{Bohm} \frac{1}{2} m_i V_i^2$$
$$- \frac{2 k T_i}{\gamma - 1}(n_i n_n < \sigma_{iz} v_e > - n_i^2 < \sigma_{rc} v_e > - n_i \sigma_{wall} V_{Bohm})$$
$$+ V_i \frac{\partial}{\partial x} 2 n_i k T_i - m_i n_i n_n < \sigma_{iz} v_e > (V_n V_i - \frac{1}{2} V_i^2) + n_i^2 < \sigma_{rc} v_e > \frac{1}{2} m_i V_i^2$$
$$- m_i n_i n_n (\sigma_{cx} V_{cx} + r_{in} + r_{ni})(V_i^2 - V_i V_n) - m_i V_i^2 n_i \sigma_{wall} V_{Bohm} \tag{A.38}$$

$$\frac{n_n}{\gamma-1}(\frac{\partial kT_n}{\partial t}+V_n\frac{\partial kT_n}{\partial x})=$$
$$-\frac{\partial}{\partial x}(V_n n_n k_{Tn})-n_i n_n<\sigma_{iz}v_e>\frac{1}{2}m_iV_n^2+n_i^2<\sigma_{rc}v_e>(\frac{1}{2}m_iV_n^2)$$
$$+n_in_n\sigma_{cx}V_{cx}m_i(V_i^2-V_n^2)+V_nm_in_in_n(V_n-V_i)r_{in}+V_im_in_in_n(V_n-V_i)r_{ni}$$
$$-n_in_nq_{iz}+n_i^2q_{rc}+n_in_n\frac{3}{4}(q_{ni}-q_{in})-n_n\sigma_{wall}\sqrt{\frac{\gamma kT_n}{m_i}}\frac{1}{2}m_iV_n^2$$
$$-\frac{kT_n}{\gamma-1}(-n_{in_n}<\sigma_{iz}v_e>+n_i^2<\sigma_{rc}v_e>+n_i\sigma_{wall}V_{Bohm})$$
$$+V_n\frac{\partial}{\partial x}(n_nkT_n)+n_in_n<\sigma_{iz}v_e>m_iV_n^2+n_i^2<\sigma_{rc}v_e>m_i(V_iV_n-\frac{1}{2}V_n^2)$$
$$+m_in_in_n(\sigma_{cx}V_{cx}+r_{in}+r_{ni})(V_n^2-V_iV_n)+m_iV_n^2\sigma_{wall}(\frac{1}{2}n_iV_{Bohm}+n_n\frac{\gamma kT_n}{m_i})$$
(A.39)

Multiply by $\frac{\gamma-1}{nk}$ and simplify

$$\frac{\partial T_i}{\partial t}=$$
$$D\frac{\partial^2V_i}{\partial x^2}-V_i\frac{\partial V_i}{\partial x}-(\gamma-1)T_i\frac{\partial V_i}{\partial x}$$
$$-\frac{1}{2}n_n<\sigma_{iz}v_e>(2T_i+(\gamma-1)\phi_{iz})+n_i<\sigma_{rc}v_e>T_i+\frac{\gamma-1}{2k}n_n(\frac{1}{2}<\sigma_{iz}v_e>$$
$$+\frac{1}{2}\sigma_{cx}V_{cx}+r_{in})m_i(V_i^2-V_n^2)+(\gamma-1)n_n<\sigma_{iz}v_e>\frac{3}{4}T_n$$
$$-(\gamma-1)n_i<\sigma_{rc}v_e>\frac{3}{4}T_i+\frac{\gamma-1}{k}m_in_n\sigma_{cx}\frac{3}{8}(q_{in}-q_{ni})+\frac{1}{2}\sigma_{wall}V_{Bohm}(2T_i-\frac{\gamma-1}{k}m_iV_i^2)$$
(A.40)

$$\frac{\partial T_n}{\partial t} =$$
$$D\frac{\partial^2 V_n}{\partial x^2} - V_n\frac{\partial V_n}{\partial x} - (\gamma-1)T_n\frac{\partial V_n}{\partial x}$$
$$+ (\gamma-1)n_i T_n(<\sigma_{iz}v_e> - \frac{n_i}{n_n}<\sigma_{rc}v_e>) + \frac{\gamma-1}{k}m_i n_i(\frac{n_i}{2n_n}<\sigma_{rc}v_e>$$
$$+ r_{ni})(V_i - V_n)^2 + \frac{\gamma-1}{k}\frac{1}{2}m_i n_i \sigma_{cx} V_{cx}(V_i^2 - 2V_iV_n - V_n^2) - (\gamma-1)n_i <\sigma_{iz}v_e> \frac{3}{2}T_n$$
$$- (\gamma-1)\frac{n_i^2}{n_n}<\sigma_{rc}v_e> \frac{3}{2}T_i + \frac{\gamma-1}{k}m_i n_i \sigma_{cx}\frac{3}{4}(q_{ni} - q_{in}) + \sigma_{wall}(\frac{\gamma-1}{k}\frac{1}{2}m_i V_n^2(\frac{n_i}{n_n}V_{Bohm}$$
$$+ \sqrt{\frac{\gamma k T_n}{m_i}}) - \frac{n_i}{n_n}V_{Bohm}T_n) \tag{A.41}$$